Cell Reports

Article

PKM2 diverts glycolytic flux in dependence on mitochondrial one-carbon cycle

Graphical abstract

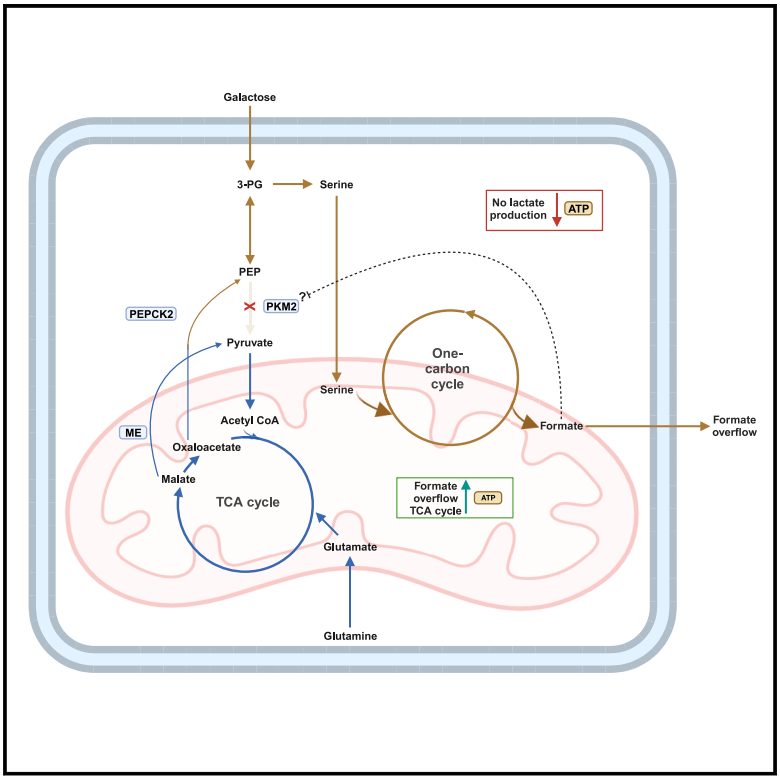

Highlights

- Galactose is a tool to mimic glycolytic limitation
- Glycolytic limitation prioritizes serine synthesis pathway (SSP) through PKM2 block
- PKM2 block requires activation of ME to maintain TCA cycle, while PEPCK2 supports SSP
- PKM2 block is independent of serine and is linked to mitochondrial 1C metabolism

Authors

Mohaned Benzarti, Laura Neises, Anais Oudin, ..., Simone P. Niclou, Elisabeth Letellier, Johannes Meiser

Correspondence

johannes.meiser@lih.lu

In brief

Benzarti et al. demonstrate that glycolytic limitation forces cancer cells to rewire their glycolytic flux toward SSP by PKM2 inhibition. PKM2 inhibition is independent of serine and can be reversed by genetic ablation of mitochondrial 1C cycle enzymes. These findings highlight cellular adaptation mechanisms upon limited carbon supply.

Benzarti et al., 2024, Cell Reports *43*, 113868
March 26, 2024
https://doi.org/10.1016/j.celrep.2024.113868

CellPress

Cell Reports

CellPress
OPEN ACCESS

Article

PKM2 diverts glycolytic flux in dependence on mitochondrial one-carbon cycle

Mohaned Benzarti,[1,2,3] Laura Neises,[1,13] Anais Oudin,[4,13] Christina Krötz,[1] Elodie Viry,[5] Ernesto Gargiulo,[5] Coralie Pulido,[6] Maryse Schmoetten,[3] Vitaly Pozdeev,[3] Nadia I. Lorenz,[7,8,9,10] Michael W. Ronellenfitsch,[7,8,9,10] David Sumpton,[11] Marc Warmoes,[12] Christian Jaeger,[12] Antoine Lesur,[1] Björn Becker,[1] Etienne Moussay,[5] Jerome Paggetti,[5] Simone P. Niclou,[2,4] Elisabeth Letellier,[3] and Johannes Meiser[1,14,*]

[1]Cancer Metabolism Group, Department of Cancer Research, Luxembourg Institute of Health, Luxembourg, Luxembourg
[2]Faculty of Science, Technology and Medicine, University of Luxembourg, Belvaux, Luxembourg
[3]Molecular Disease Mechanisms Group, Faculty of Science, Technology and Medicine, Department of Life Sciences and Medicine, University of Luxembourg, Belvaux, Luxembourg
[4]NORLUX Neuro-Oncology Laboratory, Department of Cancer Research, Luxembourg Institute of Health, Luxembourg, Luxembourg
[5]Tumor Stroma Interactions, Department of Cancer Research, Luxembourg Institute of Health, Luxembourg, Luxembourg
[6]Animal Facility, Department of Cancer Research, Luxembourg Institute of Health, Luxembourg, Luxembourg
[7]Dr. Senckenberg Institute of Neurooncology, University Hospital Frankfurt, Goethe University, Frankfurt am Main, Germany
[8]German Cancer Consortium, Partner Site Frankfurt/Mainz, Frankfurt am Main, Germany
[9]Frankfurt Cancer Institute (FCI), University Hospital Frankfurt, Goethe University, Frankfurt am Main, Germany
[10]University Cancer Center Frankfurt (UCT), University Hospital Frankfurt, Goethe University, Frankfurt am Main, Germany
[11]Cancer Research U.K. Scotland Institute, Switchback Road, Bearsden, Glasgow G61 1BD, UK
[12]Metabolomics Platform, Luxembourg Centre for Systems Biomedicine, University of Luxembourg, Belvaux, Luxembourg
[13]These authors contributed equally
[14]Lead contact
*Correspondence: johannes.meiser@lih.lu
https://doi.org/10.1016/j.celrep.2024.113868

SUMMARY

Modeling tumor metabolism *in vitro* remains challenging. Here, we used galactose as an *in vitro* tool compound to mimic glycolytic limitation. In contrast to the established idea that high glycolytic flux reduces pyruvate kinase isozyme M2 (PKM2) activity to support anabolic processes, we have discovered that glycolytic limitation also affects PKM2 activity. Surprisingly, despite limited carbon availability and energetic stress, cells induce a near-complete block of PKM2 to divert carbons toward serine metabolism. Simultaneously, TCA cycle flux is sustained, and oxygen consumption is increased, supported by glutamine. Glutamine not only supports TCA cycle flux but also serine synthesis via distinct mechanisms that are directed through PKM2 inhibition. Finally, deleting mitochondrial one-carbon (1C) cycle reversed the PKM2 block, suggesting a potential formate-dependent crosstalk that coordinates mitochondrial 1C flux and cytosolic glycolysis to support cell survival and proliferation during nutrient-scarce conditions.

INTRODUCTION

Increased aerobic glycolysis has been identified as a characteristic of cancer cells a century ago and subsequently highlighted as a hallmark of cancer.[1–4] Many theories have been suggested to explain the selective advantage of this phenotype with the majority of these theories circulating around the idea that mitochondria are unable to cope with very high rates of early glycolytic reactions that are driven by oncogenic signaling.[5–10] In these early steps of glycolysis, NAD^+ and ATP are consumed and need to be regenerated for glycolysis to continue. This regeneration of NAD^+ and ATP seems to be the decisive bottleneck where cancer cells have to decide whether to ferment glucose or oxidize it fully in the TCA cycle.[9,11–13] Indeed, two recent publications highlighted how aerobic glycolysis rates are decided based on NADH shuttle capacity and the regeneration of NAD^+[12,13]. Moreover, it was proposed that cells downregulate mitochondrial respiration to avoid ATP depletion when the mitochondria are unable to replenish ATP used in the early steps of glycolysis fast enough. Therefore, cells turn to ATP generation via lactate overflow to avoid an ATP crisis.[4,9,11]

While it has been suggested that aerobic glycolysis is not the main driver of high proliferation rates,[13] it remains undeniable that cancer cells engage high proliferative rates in favorable metabolic environments with ampleness of glucose being an example of such environments. Therefore, *in vitro*, it might seem that cancer cells are fixed on aerobic glycolysis, while *in vivo*, they actually display metabolic flexibility and plasticity.[14] This is to survive nutrient-depleted and hostile metabolic environments within the local tumor microenvironment (TME) and along the metastatic cascade.[15] However, such metabolic flexibility is usually masked within *in vitro* studies due to the usage of

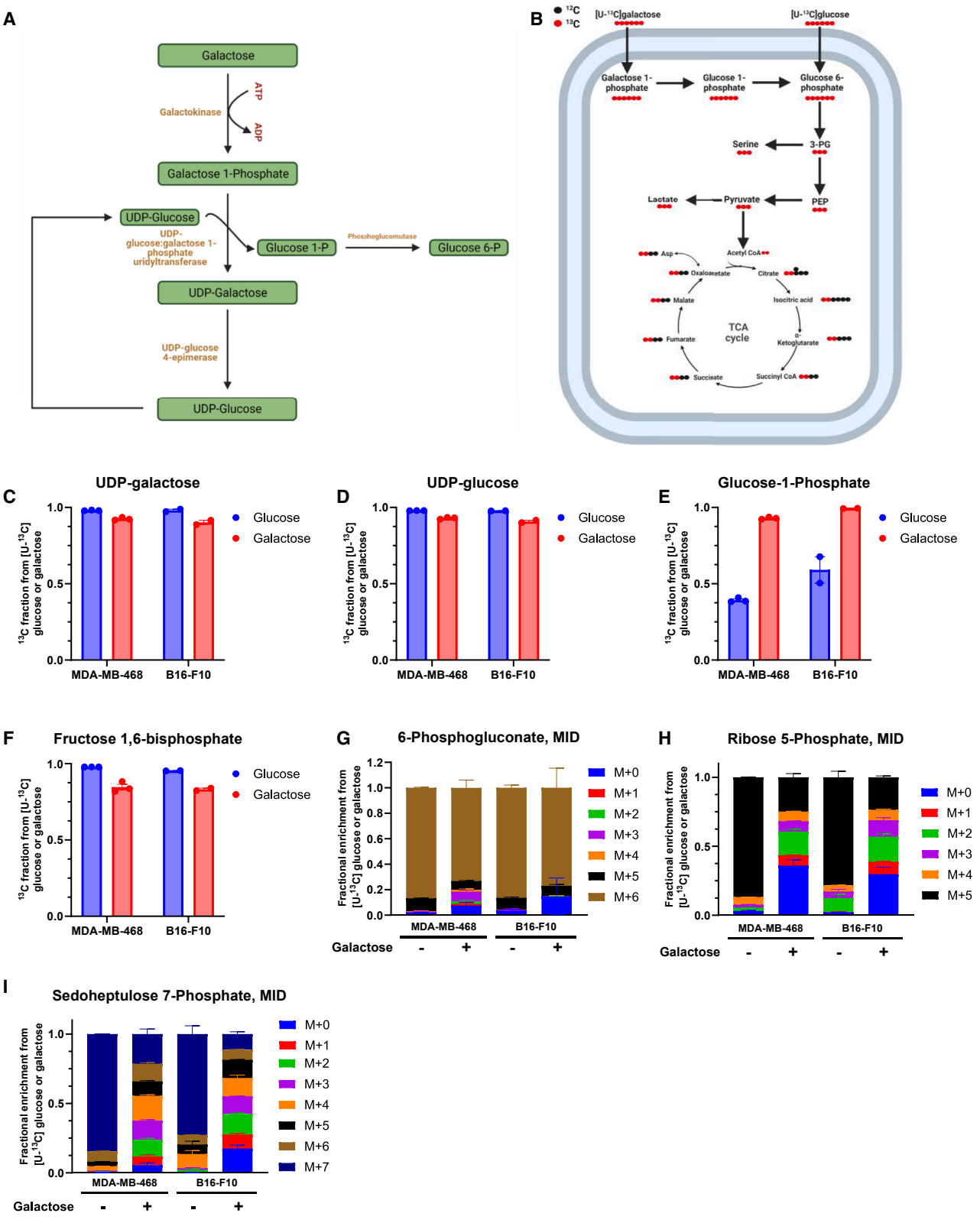

(legend on next page)

synthetic media containing supraphysiological concentrations of various metabolites.[16] Aerobic glycolysis can be caused *in vitro* as cancer cells become reversibly addicted to glycolysis and repress their mitochondrial respiration in response to high glucose concentration in their respective media i.e., the Crabtree effect.[11,17]

One method to circumvent this glycolytic addiction and to unmask cancer cells' metabolic flexibility *in vitro* is to substitute glucose for galactose. Galactose is metabolized via the Leloir pathway to produce glucose 6-phosphate (G6P), meaning that it can support glycolysis.[18] While glucose is converted into G6P in a one-step reaction by hexokinase (Km $\sim$ 0.3 mM),[19,20] galactose requires four biochemical reactions to continuously supply the cell with G6P with the initial reaction catalyzed by galactokinase having a Km value three times higher than hexokinase (galactokinase Km $\sim$ 1 mM).[21] This results in galactose providing a slow, yet continuous, supply of carbons, mimicking the TME where glucose is rapidly consumed but continuously being replenished via circulation.[22,23] Therefore, we used galactose as an *in vitro* tool compound to mimic glycolytic limitation that occurs within the TME.

We have previously shown that cancer cells increase serine catabolism and formate overflow under glycolytic limitation even though biosynthetic demands were decreased,[24] indicating also a growth-independent role of one-carbon (1C) metabolism.[25,26] Moreover, it has been shown that glutamine can support serine synthesis pathway (SSP) under glucose starvation via phosphoenolpyruvate carboxykinase 2 (PEPCK2).[27–30] Both observations indicate that metabolic rewiring takes place toward SSP under glycolytic limitation, yet the exact mechanisms and metabolic advantages of this rewiring remain unclear. Building on these observations, we performed deep metabolic phenotyping to study the rewiring that takes place under glycolytic limitation. We observed a continued but decreased flux through glycolysis while oxygen consumption rates (OCRs) were increased.[24] Surprisingly and despite increased OCR, galactose-derived carbons did not enter the TCA cycle for mitochondrial oxidation, suggesting that glutamine is the main substrate to support the TCA cycle in these conditions. This is facilitated by a strong pyruvate kinase isozyme M2 (PKM2) block, pinpointing PKM2 as the rewiring node and facilitating carbon shunting toward SSP. Finally, we observed an upregulation of the mitochondrial 1C enzymes to support biosynthesis, bioenergetics, and redox balance under glycolytic limitation. Interestingly, loss of mitochondrial 1C flux resulted in a re-shunting of galactose-derived carbon toward the TCA cycle at a similar level compared to the PKM2 activator TEPP-46. While the complete mechanism remains unclear and needs follow-up work, our findings pinpoint a sensing mechanism that coordinates mitochondrial 1C flux and cytosolic glycolysis.

RESULTS

Cancer cells metabolize galactose and utilize it to support early glycolysis

To ascertain that cancer cells are able to metabolize galactose (Gal), we used a fully labeled [U-^{13}C]Gal or [U-^{13}C]glucose (Glc) tracer and compared the relative fluxes through the Leloir pathway (Figure 1A) and early glycolysis (Figure 1B). The relative flux to UDP-glucose and UDP-galactose was comparable between Glc and Gal tracing and even higher in the case of glucose 1-phosphate in Gal (Figures 1C–1E for the full ^{13}C fraction; Figures S1A–S1C for the individual isotopologues). The ^{13}C enrichment of fructose 1,6-bisphosphate (FBP) was comparable between both tracers, suggesting a similar relative flux of Glc and Gal (Figures 1F and S1D). Of note, the absolute consumption rate of Gal was strongly reduced compared to Glc, which is also reflected in the intracellular levels of early glycolytic and pentose phosphate pathway (PPP) metabolites (Figure S1E). With both tracers, we observed high ^{13}C enrichment in the early PPP intermediate 6-phosphogluconate (Figure 1G). However, especially the isotopologue pattern in ribose 5-phosphate (R5P) and sedoheptulose 7-phosphate (S7P) showed a more scattered distribution indicating higher shunting of carbons between PPP, early glycolysis, and gluconeogenesis in Gal conditions (Figures 1H and 1I). Overall, these data demonstrate that cancer cells are able to utilize Gal to fuel early glycolysis and PPP intermediates through the Leloir pathway.

Glutamine and lactate maintain an upregulated oxidative TCA cycle function under glycolytic limitation

Glycolytic limitation has been reported to promote mitochondrial metabolism reflected in increased OCR (Figure S2A) and increasing glutamine usage.[24,30,31] To test if this is also the case upon limited glycolytic flux (compared to full starvation), we measured sustained glutamine consumption despite decreased growth rates suggesting that an increased fraction of glutamine is catabolized through the TCA cycle instead of being used for anabolic metabolism (Figures 2A and S2B). This assumption was corroborated with [U-^{13}C]glutamine tracing, revealing an increased relative flux from glutamine into the TCA cycle (Figures 2B–2D). Moreover, performing [^{15}N-amine]glutamine tracing showed increased activity of transamination reaction under glycolytic limitation (Figure S2C). Under Glc, we observed that glutamine enrichment in the TCA cycle metabolites decreased as we moved away from glutamine. In contrast, the enrichment remains unchanged under Gal (Figures 2B–2D), indicating that the TCA cycle is running with strongly reduced carbon input from glycolysis. Yet, acetyl-CoA input is required to sustain glutamine oxidation through the TCA cycle, hinting

Figure 1. Cancer cells metabolize galactose and utilize it to support early glycolysis

(A) Schematic representation of Leloir pathway for galactose metabolism.

(B) Schematic representation of the expected labeling pattern of simplified central carbon metabolism when using [U-^{13}C]glucose and [U-^{13}C]galactose tracer.

(C–F) ^{13}C fraction from [U-^{13}C]glucose and [U-^{13}C]galactose into UDP-galactose (C), UDP-glucose (D), glucose 1-phosphate (E), and fructose 1,6-bisphosphate (F) after 24-h incubation. Each dot represents an independent experiment averaged from 3 different replicate wells.

(G–I) Fractional enrichment in 6-phosphogluconate (G), ribose 5-phosphate (H), and sedoheptulose 7-phosphate (I) from [U-^{13}C]glucose and [U-^{13}C]galactose after 24-h incubation. Data shown are mean ± SEM of 3 (MDA-MB-468) or 2 (B16-F10) independent experiments, each being the average of 3 different replicate wells.

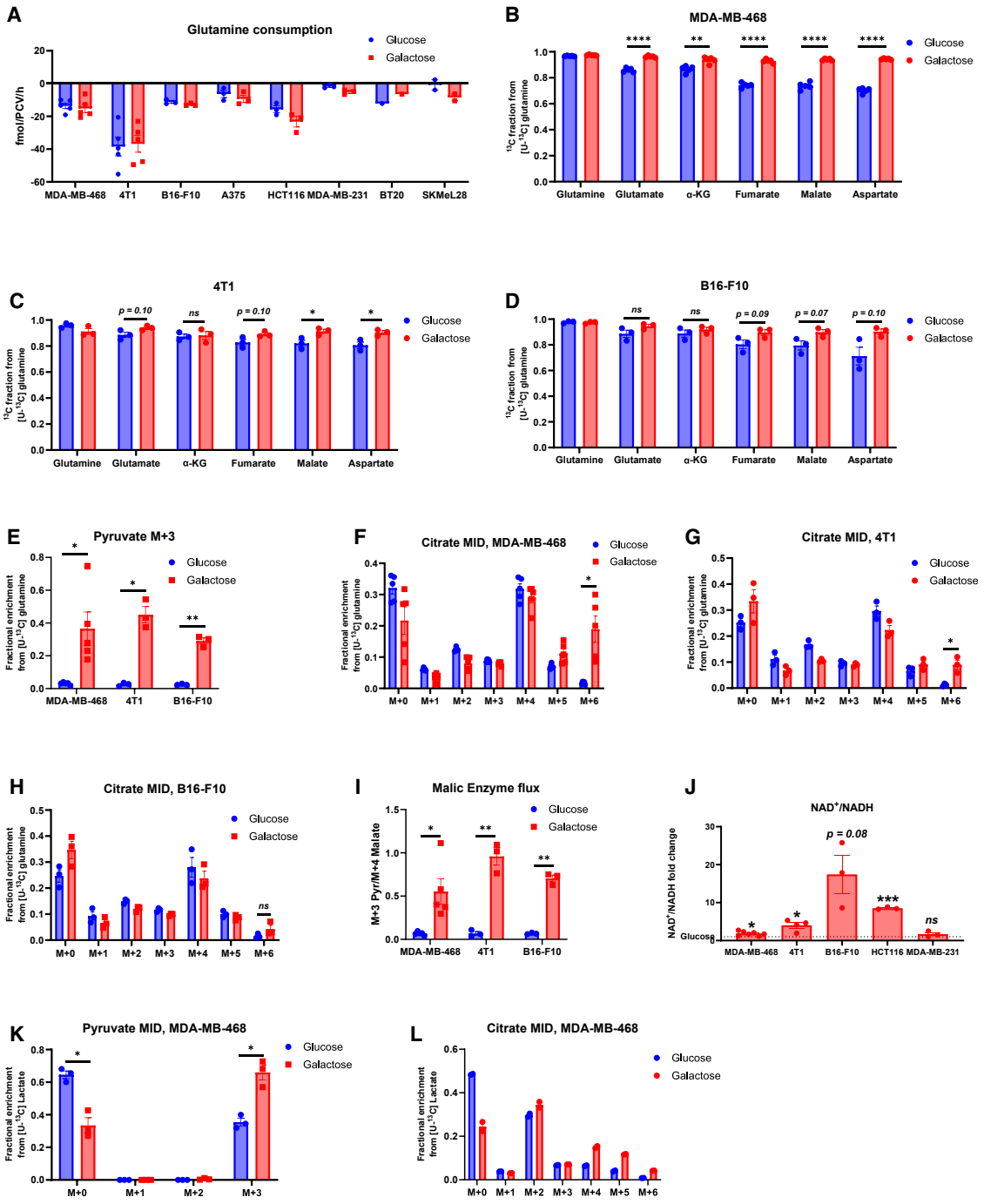

Figure 2. Glutamine and lactate maintain upregulated oxidative TCA cycle function in reliance on malic enzyme (ME)

(A) Absolute quantification of glutamine consumption from multiple cancer cell lines after 24-h incubation with either glucose or galactose medium.

(B–D) ^{13}C fraction in TCA cycle metabolites from [U-^{13}C]glutamine after 24-h incubation with either glucose or galactose medium in MDA-MB-468 (B), 4T1 (C), and B16-F10 (D).

(E) Fractional enrichment in M+3 pyruvate from [U-^{13}C]glutamine after 24-h incubation with either glucose or galactose medium in MDA-MB-468, 4T1, and B16-F10.

(F–H) Fractional enrichment in citrate from [U-^{13}C]glutamine after 24-h incubation with either glucose or galactose medium in MDA-MB-468 (F), 4T1 (G), and B16-F10 (H).

(I) Malic enzyme flux ratio calculated as M+3 pyruvate/M+4 malate isotopologues from [U-^{13}C]glutamine after 24-h incubation with either glucose or galactose medium in MDA-MB-468, 4T1, and B16-F10.

(legend continued on next page)

toward malic enzyme (ME) activity to sustain pyruvate levels under glycolytic limitation. ME decarboxylates malate into pyruvate, and indeed, we observed a substantial M+3 labeling of pyruvate and lactate from [U-^{13}C]glutamine under glycolytic limitation (Figures 2E and S2D). ME involvement is further supported by increased citrate M+6 isotopologue abundance (Figures 2F–2H). On these lines, the ratio of M+3 pyruvate/M+4 malate (ME flux) was also increased (Figure 2I). These findings display the metabolic plasticity of cancer cells, as they are able to rewire their metabolism to run the TCA cycle mainly on glutamine. However, we are still able to detect an unlabeled fraction in citrate (Figures 2F–2H), which is partially derived from fatty acid oxidation as measured by [U-^{13}C]palmitate (Figure S2E).

An additional carbon source that we might neglect with our *in vitro* setup is lactate, whose build-up is a prominent feature of most solid tumors.[32] In fact, recent evidence from *in vivo* studies suggests that lactate can be a major carbon source to the TCA cycle of cancer cells.[33,34] To test if this feature can be recapitulated in our *in vitro* model, we performed [U-^{13}C]lactate tracing at a concentration of 5 mM, as this was indicated as a physiological relevant concentration within the TME.[22,35] Supported by the increase in NAD$^+$/NADH ratio (Figure 2J), we observe a net uptake of lactate and increased ^{13}C contribution from lactate to pyruvate and the TCA cycle via PDH (Figures 2K, 2L, and S2F–S2I). In summary, we conclude that alternative carbon sources can substitute for Glc to support and run lower glycolysis and the TCA cycle independently. Importantly, the sustained flux through PDH (Figure S2I) suggests that a block upstream of PDH prevents glycolysis-derived entry into the TCA cycle.

Glutamine metabolism is redirected toward SSP under glycolytic limitation via PEPCK2

It has previously been shown that under full Glc starvation, gluconeogenesis enzyme PEPCK2 becomes active and supports the biosynthesis of glycolytic intermediates.[27–30,36] To test if this is also the case in Gal and not only upon full hexose starvation, we monitored glutamine-derived carbon contribution to phosphoenolpyruvate (PEP) and 3-PG (Figures S3A and S3B). Overall, we were able to confirm PEPCK activity in three different cancer cell lines with up to 30% of the measured serine being fully labeled under serine/glycine (SG) starvation (Figure 3A). Even with SG in the medium, the glutamine flux to serine under Gal was comparable to the one from Glc (Figure 3B). Conclusively, we also observed glutamine-derived ^{13}C enrichment in ATP (Figure 3C), glutathione (GSH) (Figure 3D), and formate (Figure S3C), further indicating upregulation of PEPCK activity (Figure 3E). Of note, the labeled fraction of ATP reached an astonishing 40%–50% under SG starvation in all three cell lines (Figure 3C).

Mitochondrial PEPCK (PEPCK2) has been identified as the major isoform present in most tumor tissues.[27] Here, we observed that PEPCK2 protein expression was markedly increased under glycolytic limitation (Figure S3D). Subsequently, we used two different genetic approaches to silence PEPCK2 (Figures S3E and S3F), confirming PEPCK2 as the culprit for the glutamine-derived ^{13}C enrichment in serine, ATP, and GSH (Figures 3F–3I). Importantly, intracellular serine levels significantly dropped in MDA-MB-468 and 4T1 but not in B16-F10 cells (Figure 3G), indicating the importance of the glutamine flux for the serine pool while also highlighting cell-line-dependent strategies to control serine levels (Figure 3G). Furthermore, we observed a mild increase in the labeling of TCA cycle intermediates and pyruvate from glutamine in PEPCK2 (knockdown/knockouts) KD/KOs, which most likely is a result of the elimination of the flux through PEPCK (Figures S3H and S3I). However, loss of PEPCK2 did not affect proliferation rates (Figures 3J, S3J, and S3K), indicating compensatory mechanisms. Yet, neither fractional contribution from Gal nor serine consumption was significantly increased in PEPCK2 KD/KOs (Figures S3L–S3O).

In sum, we show that upon glycolytic limitation, glutamine metabolism is rewired to increase its catabolism through the TCA cycle and to support SSP in a PEPCK2-dependent manner (Figure 3K). However, it remains unclear how PEPCK2 and ME fluxes are coordinated as these fluxes cannot be disentangled by using [U-^{13}C]glutamine.

Cancer cells favor carbon flux toward SSP under glycolytic limitation

To study the relative fluxes of lower glycolysis in more detail, we traced [U-^{13}C]Gal in a panel of nine different cancer cell lines representing four different tumors (breast, colorectal, glioblastoma, and melanoma). Despite similar enrichment in FBP (Figure 1F), the relative flux decreased toward late glycolytic intermediates with especially pyruvate showing only about 10% of the ^{13}C enrichment observed under Glc, which could be explained partly by the increased flux from [U-^{13}C]glutamine under Gal (Figures 4A–4C). In comparison, cells appeared to keep about 25%–50% of their relative flux toward serine under Gal (Figure 4C). The strong reduction in ^{13}C incorporation in pyruvate appeared robust as neither different time points, different Glc/Gal concentrations, dialyzed serum, or different media (RPMI or Plasmax[37]) impacted this result (Figures S4A–S4D), suggesting that the different labeling pattern in pyruvate originates from an adaptation of central carbon metabolism. To eliminate the possibility of an inhibitory action of Gal, we mixed Glc and Gal in a 1:1 mix where the Glc added was ^{13}C. If Gal had a direct inhibitory action on glycolysis, we would expect to see a clear reduction of ^{13}C flux toward pyruvate; however, we observed no difference in ^{13}C enrichment in glycolysis under such conditions (Figure S4E). These observations indicate that the reduced glycolytic ^{13}C flux is a result of the cells' response to the limited availability of carbons under Gal.

To better visualize the differences between the relative flux toward lower glycolysis and SSP, we used 3-PG (divergent point between SSP and lower glycolysis) M+3 isotopologue as a common denominator to normalize the main labeled isotopologue of

(J) NAD$^+$/NADH ratio measured with liquid chromatography-mass spectrometry (LC-MS) in the indicated cancer cell lines after 24-h incubation with galactose and normalized to the same ratio with 24-h incubation with glucose medium.
(K and L) Fractional enrichment in pyruvate (K) and citrate (L) from 5 mM [U-^{13}C]sodium lactate after 24-h incubation with either glucose or galactose medium in MDA-MB-468. (A–L) Each dot represents an independent experiment averaged from 3 different replicate wells unless stated otherwise. Mean ± SEM, *$p < 0.05$, **$p < 0.01$, ***$p < 0.001$, ****$p < 0.0001$, ns $p > 0.1$. p value is calculated by Student's t test, two-tailed, unpaired with Welch's correction unless stated otherwise.

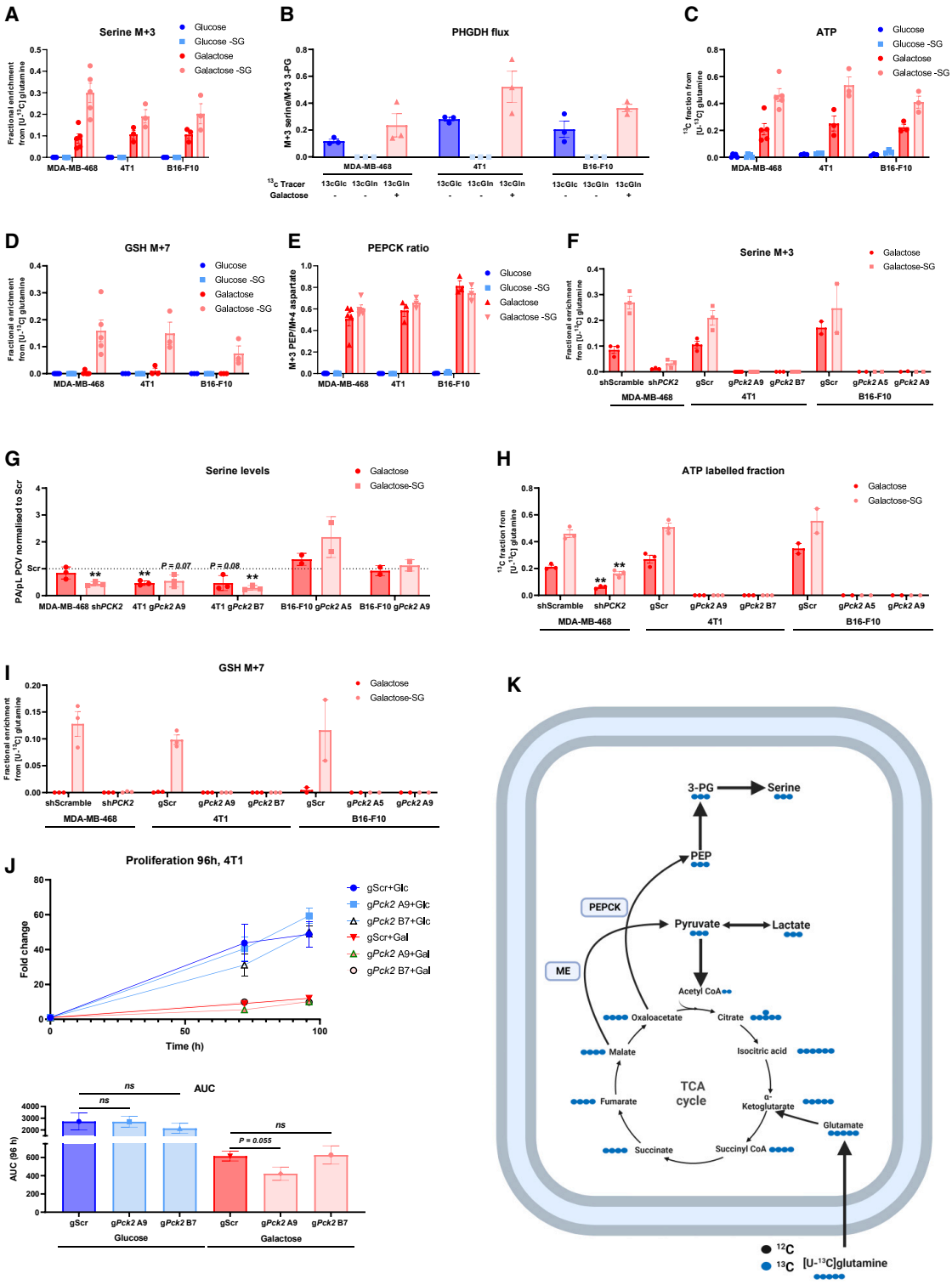

Figure 3. Glutamine metabolism is redirected toward SSP under glycolytic limitation via PEPCK

(A) Fractional enrichment in M+3 serine from [U-^{13}C]glutamine after 24-h incubation with either glucose ± serine and glycine (SG) or galactose ± SG medium in MDA-MB-468, 4T1, and B16-F10.

(B) Phosphoglycerate dehydrogenase (PHGDH) enzyme flux ratio calculated as M+3 serine/M+3 3-PG isotopologues from [U-^{13}C]glucose or glutamine (either with glucose or galactose medium) after 24-h incubation in MDA-MB-468, 4T1, and B16-F10.

(legend continued on next page)

different metabolites (e.g., M+3 serine/M+3 3PG, M+3 pyruvate/M+3 3PG, M+2 citrate/M+3 3PG, etc.). The resulting ratios are presented as a fold change of the same ratios under Glc (Figures 4D and 4E). We found that in most cell lines, the relative ratio for serine under Gal was comparable or higher than under Glc, indicating comparable or higher relative flux to SSP under glycolytic limitation. In contrast, the relative ratio for pyruvate was strikingly lower under Gal. Thus, we observed that cancer cells rewire their limited ^{13}C supply under Gal toward SSP, thereby reducing the carbon supply to lower glycolysis. This effect also resulted in lower pyruvate but rather sustained intracellular serine levels (Figures 4F and 4G). Interestingly, cell lines that doubled under 24 h (fast growing) (Figures 4D and 4E) showed a more abundant phenotype. One exception was the murine breast cancer cell line 4T1, which is extremely glycolytic and is very sensitive to Gal, indicating that this cell line may not be able to adapt to such an environment (Figure 4E). Subsequently, we validated the rewiring phenotype also in the physiological Plasmax medium (Figure 4H). When ^{13}C-Glc was mixed 1:1 with ^{12}C-Gal, we saw that there was no change in the ^{13}C flux ratios, showing again that Gal is not inhibitory of glycolysis (Figure 4I). However, when ^{13}C-Gal was mixed with ^{12}C-Glc, we saw that the flux was heavily favored toward pyruvate and lactate and not to SSP (Figure 4I), indicating that this rewiring only takes place when glycolytic carbon is limited.

Glycolytic limitation inhibits glycolysis at PKM2 independently of serine levels

To understand the driving force that redirects the limited available carbon toward SSP, we first looked at protein abundance of SSP enzymes. However, we did not observe striking changes at the protein and mRNA level (Figures S4F and S4G). We suggest that the sustained flux through SSP is likely a more direct metabolic adaptation favored by the increased NAD^+/NADH ratio (Figure 2J), which is known to promote SSP.[38]

However, in addition to this "RedOX effect," we were curious to understand why we observed the strong loss of ^{13}C incorporation between PEP and pyruvate (Figure 5A). Supported by PEP accumulation (Figure 5B), we hypothesized that PKM2, a known regulatory node of glycolysis,[39] may be inhibited (Figure 5A). A PKM2 block could further explain the observed loss of lactate secretion under Gal (Figure S5A) as well as loss of ^{13}C labeling in pyruvate but not in PEP (Figures 5C, S5B, and S5C). To test if we can increase PKM2 activity, we used the PKM2 activator TEPP-46.[40] Indeed, the activation of PKM2 increased the ^{13}C flux toward citrate at the cost of serine synthesis (Figure 5D). Furthermore, TEPP-46 caused a complete loss of serine labeling from [U-^{13}C] glutamine, indicating that the rewiring into SSP depends on PKM2 inhibition (Figure S5D). At a functional level, PKM2 activation decreased proliferation both in 2D and 3D (Figures 5E and S5E), suggesting that PKM2 inhibition is crucial in cells suffering from limited carbon availability for glycolysis (Figure 5E).

FBP binds to PKM2 and induces the formation of the active tetramer form.[41,42] To test if FBP reduction (Figure S5F) is causing the PKM2 inhibition, we titrated FBP to increase intracellular FBP concentrations (Figure S5G). Potentially, supraphysiologic FBP levels (when adding 20 mM into the medium) may impact the rewiring; however, we saw no clear restoration of pyruvate oxidation into the TCA cycle (compared to TEPP-46) (Figure S5H). Of note, this experiment is not 100% conclusive as ^{12}C-FBP can dilute the ^{13}C signal coming from Gal. Nonetheless, *in vitro* biochemical studies have shown that isolated PKM2 can remain active even in the complete absence of FBP,[42,43] suggesting that the drop in FBP is not the sole cause of PKM2 inhibition. Reactive oxygen species (ROS) have also been shown to inactivate PKM2.[44] Yet, in our setup, we observed no increase in ROS (Figures S5I and S5J) nor did antioxidant treatment impact the rewiring (Figure S5K).

Finally, serine has been shown to act as allosteric activator of PKM2.[45] However, in our experimental setup, serine levels are maintained (Figure 4G). To further investigate if alteration of serine levels can impact PKM2 activity, we utilized PEPCK2 KD cells, which have reduced serine levels (Figures 3G and 5F). When PEPCK2 KD cells were cultured in SG starvation leading to a further drop of serine levels (Figure 5F), M+2 citrate isotopologues remained unchanged (Figure 5G). Lastly, combining S/G starvation with the competitive inhibitor of PHGDH (to block SSP) BI-4916[46] strongly diminished the intracellular pool of serine (Figure 5F). Unexpectedly, however, this led to restoring the glycolytic flux into the TCA cycle, likely by containing the Gal-derived carbon in glycolysis (Figure 5G). In sum, the

(C) ^{13}C fraction in ATP from [U-^{13}C]glutamine after 24-h incubation with either glucose ± SG or galactose ± SG medium in MDA-MB-468, 4T1, and B16-F10.
(D) Fractional enrichment in M+7 glutathione (GSH) from [U-^{13}C]glutamine after 24-h incubation with either glucose ± SG or galactose ± SG medium in MDA-MB-468, 4T1, and B16-F10.
(E) Phosphoenolpyruvate carboxykinase (PEPCK) enzyme flux ratio calculated as M+3 PEP/M+4 aspartate isotopologues from [U-^{13}C]glutamine after 24-h incubation with either glucose ± SG or galactose ± SG medium in MDA-MB-468, 4T1, and B16-F10.
(F) Fractional enrichment in M+3 serine from [U-^{13}C]glutamine after 24-h incubation with galactose ± SG medium in MDA-MB-468 shScramble and sh*PCK2* cells, 4T1, and B16-F10 gScramble and g*Pck2* cells.
(G) Peak areas (PAs) of intracellular serine in PEPCK2 KD/KOs normalized to packed cell volume (PCV) in picoliters (pL) and presented as fold change to the levels in scramble cells. Data shown are for the levels measured in galactose ± SG medium.
(H) ^{13}C fraction in ATP from [U-^{13}C]glutamine after 24-h incubation with galactose ± SG medium and the comparison between scramble and PEPCK2 KD/KOs cells.
(I) Fractional enrichment in M+7 glutathione (GSH) from [U-^{13}C]glutamine after 24-h incubation with galactose ± SG medium and the comparison between scramble and PEPCK2 KD/KO cells.
(J) 2D proliferation curve of 4T1 gScramble and g*Pck2* cells with either glucose or galactose, with the corresponding area under the curve (AUC). 72-h time point includes 3 independent experiments, while 96-h time point includes 4 independent experiments (from at least 3 different replicate wells for each independent experiment). (A–J) Each dot represents an independent experiment averaged from 3 different replicate wells unless stated otherwise. Mean ± SEM, *$p < 0.05$, **$p < 0.01$, ***$p < 0.001$, ****$p < 0.0001$, ns $p > 0.1$. p value is calculated by Student's t test, two-tailed, unpaired with Welch's correction unless stated otherwise.
(K) Schematic representation of the rewiring of glutamine metabolism that takes place under glycolytic limitation.

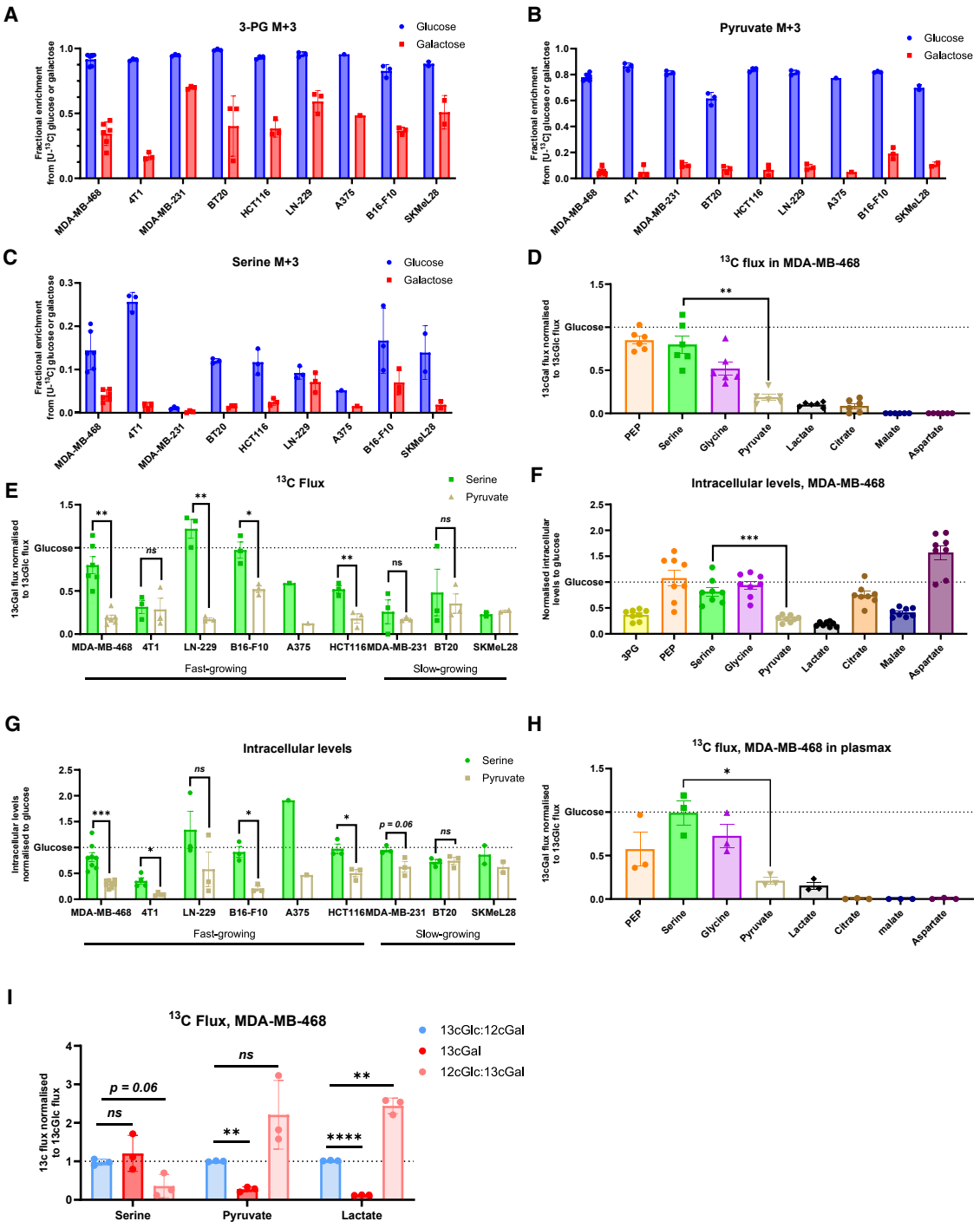

Figure 4. Cancer cells sustain carbon flux toward serine synthesis pathway (SSP) under glycolytic limitation

(A–C) Fractional enrichment from 17.5 mM [U-^{13}C]glucose and galactose into M+3 3PG (A), M+3 pyruvate (B), and M+3 serine (C) after 24-h incubation measured with LC-MS.

(D and E) The normalized relative ^{13}C flux under galactose toward multiple metabolites represented as a fold change of the same ratio under glucose in MDA-MB-468 (D) and a panel of 9 cancer cell lines (E). Fast-growing cells are those with doubling time <24 h.

(F and G) Intracellular levels of multiple metabolites under galactose represented as a fold change of the levels under glucose in MDA-MB-468 (F) and a panel of 9 cancer cell lines (G).

(legend continued on next page)

observed block of PKM2 is independent of serine levels (Figure 5H).

SSP drives serine catabolism and formate production, which impacts PKM2 activity

To understand the selective advantage of sustained SSP under limited carbon supply, we performed functional assays and targeted PHGDH, the rate limiting enzyme of SSP. Overall, we observed that targeting PHGDH in Gal further reduced proliferative capacity both in 2D and 3D and increased apoptosis (Figures S6A–S6G), suggesting that SSP exerts a pro-proliferative and anti-apoptotic role under glycolytic limitation.

In addition to serine synthesis itself, we were interested to characterize the metabolic sinks of serine in context of glycolytic limitation (Figure 6A).[25] Toward this end, we analyzed the expression of the different enzymes of the 1C cycle and found that specifically the mitochondrial 1C enzymes showed increased expression (Figures 6B–6D). The product of the mitochondrial 1C cycle branch is formate, and we have previously shown that serine catabolism and formate overflow increase upon Gal.[24] In line with these previous results, we observed increased formate release in a panel of cancer cell lines (Figure 6E). Concurrent increased expression of ALDH1L2 alongside increased formate overflow indicates strongly increased mitochondrial 1C flux. Similar to lactate overflow, formate overflow produces one ATP molecule per MTHFD1L reaction. In addition to ATP production, formate overflow yields one NADH molecule via MTHFD2.[47] The coupling of MTHFD2-derived NADH to the electron transport chain thereby contributes to mitochondrial ATP production and the observed increase in OCR upon Gal (Figure S2A).[24] Meaning that the increased formate release can serve a crucial bioenergetic function by supporting mitochondrial ATP production under glycolytic limitation.[24] We have previously shown that under glycolytic limitation, AMPK is activated alongside the increased formate release,[24] which is an observation we could also confirm in the glioblastoma cell line LN-229 (Figure S7A). To test whether AMPK is in causal relation to SSP and 1C cycle upregulation, we used an AMPK KO cell line with both alpha subunits deleted (Figure S7B).[48] However, loss of AMPK did not reduce formate release (Figure S7C) or impact ^{13}C flux rewiring (Figure S7D), indicating that under these conditions, AMPK is not directly involved in SSP and 1C cycle upregulation. Furthermore, sole deletion of MTHFD1L did not strongly reduce 2D and 3D proliferation, indicating that loss of MTHFD1L-derived ATP production is not essential in these experimental conditions. (Figures S7E–S7G).

An alternative to formate release, formate can also support *de novo* purine and pyrimidine synthesis (anabolic role) or can be oxidized to CO_2 via ALDH1L2 or ALDH1L1 while generating NADPH (RedOx role) (Figure 6A). We explored both biosynthesis and redox balance as potential sinks for the rewired ^{13}C flux. Since we only observed a strong upregulation of ALDH1L2, we hypothesized that 1C metabolism is mostly involved in maintaining mitochondrial rather than cytosolic redox state. Moreover, when we cultivated the highly glycolytic breast cancer cell line 4T1 (Figure S5A) for 72 h in Glc without medium change, we saw that the expression of ALDH1L2 increased as Glc concentration became limited (Figure 6F). However, knocking out ALDH1L2 (Figure S7H) resulted only in mildly reduced proliferation under glycolytic limitation in both 2D and 3D assays (Figures 6G and 6H). Surprisingly, simultaneous silencing of both MTHFD1L and ALDH1L2 did not further decrease proliferation (Figures S7I and S7J).

PPP is a key regulator of biosynthesis and redox balance as it supplies the cells with R5P and NADPH.[49] The cycling of carbons we observed (Figures 1H and 1I) suggests that PPP is shifted toward maximizing the production of NADPH and R5P from the limited carbon supply under Gal. Due to this carbon cycling in PPP and subsequent labeling of R5P, it is not possible to determine the contribution of 1C metabolism to nucleotide biosynthesis by using [U-^{13}C]Glc and Gal tracers (Figures 6I and S7K–S7N). Therefore, we utilized a [U-^{13}C]serine tracer and observed that the flux from serine toward nucleotide biosynthesis is sustained under glycolytic limitation (Figure 6J). Conclusively, this suggests the idea that the flux through the mitochondrial 1C cycle serves multiple metabolic purposes and can be adapted in a context-dependent manner.

To test if mitochondrial 1C metabolism is involved in controlling the metabolic adaptation we observed in context of glycolytic limitation, we performed [U-^{13}C]Gal tracing in MTHFD1L and MTHFD2 KO cells (Figures S7H and S7I). Interestingly, we observed that loss of mitochondrial 1C flux increases ^{13}C contribution to the TCA cycle (Figures 6K, 6L, S7O, and S7P) to a similar extent compared to the PKM2 activator TEPP-46 (Figure 5D). This effect was clearest in MTHFD1L KO, while loss of ALDH1L2 had no effect. This result aligns with our observation that suppression of formate overflow via SG starvation and PHGDH inhibition also restored the Gal-derived ^{13}C flux into the TCA cycle (Figure 5G). Overall, these observations suggest that the mitochondrial 1C pathway and its product formate contribute to the rewiring of lower glycolysis and inhibition of PKM2.

Put together, it is apparent that the rewiring toward SSP and the plasticity of 1C metabolism under glycolytic limitation serves different metabolic pillars with sustained carbon flux from serine to purines and increased ATP and NADPH generation through MTHFD1L and ALDH1L2, respectively. In particular, the rate of mitochondrial serine catabolism needs to be increased, as an increased fraction of 1C units is likely to be oxidized by ALDH1L2, while at the same time, formate overflow through MTHFD1L is also increased. Additionally, cytosolic formate is required for nucleotide biosynthesis to sustain proliferation. Finally, we observed that loss of mitochondrial 1C pathway activity results in 13C carbon re-entry through PKM2 toward the TCA cycle.

(H) The normalized relative ^{13}C flux under galactose toward multiple metabolites represented as a fold change of the same ratio under glucose in MDA-MB-468 when cultured in physiological medium Plasmax.

(I) The normalized relative ^{13}C flux under galactose and glucose:galactose mixes toward multiple metabolites represented as a fold change of the same ratio under glucose in MDA-MB-468. (A–I) Each dot represents an independent experiment (from 3 different replicate wells). Mean ± SEM, *$p < 0.05$, **$p < 0.01$, ***$p < 0.001$, ****$p < 0.0001$, ns $p > 0.1$. p value is calculated by Student's t test, two-tailed, unpaired with Welch's correction.

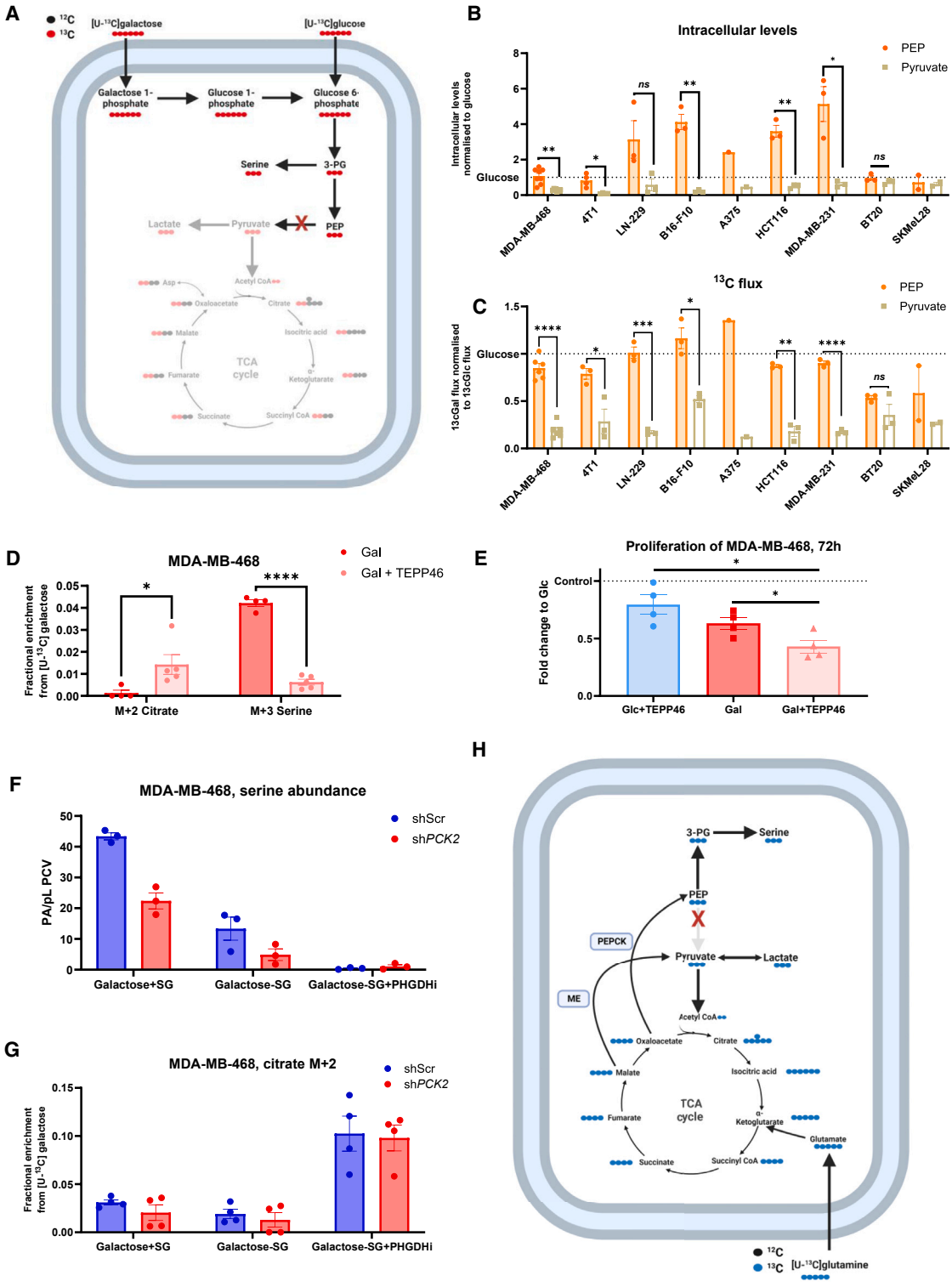

Figure 5. Glycolytic limitation inhibits glycolytic flux at pyruvate kinase isozyme M2 (PKM2)

(A) Schematic representation of glycolysis and TCA cycle upon isotopologue labeling with [U-^{13}C]glucose and galactose with the proposed block at PKM2.

(B) Intracellular levels of PEP and pyruvate under galactose represented as a fold change of the levels under glucose in a panel of 9 cancer cell lines.

(C) The normalized relative ^{13}C flux under galactose toward PEP and pyruvate represented as a fold change of the same ratio under glucose in a panel of 9 cancer cell lines.

(legend continued on next page)

Relevance of using Gal *in vitro* to model glycolytic limitation

The *in vitro* modeling of the metabolic environment that cancer cells face *in vivo* is extremely challenging due to the heterogeneity of the tumor tissue and the varying metabolite composition of the TME. To test the physiological relevance of using Gal as an *in vitro* tool compound to model glycolytic limitation *in vivo*, we subcutaneously injected B16-F10 cells into the flanks of C57BL/6 mice. We then allowed the tumors to grow for 16 and 9 days, thereby generating larger and smaller tumors, respectively (Figures 7A and 7B). Subsequently, we infused the mice with [U-^{13}C]Glc. Next, we performed targeted metabolomics and compared the small tumors to the inside and the outside of the big tumors to measure the gradient of metabolite levels between the outer layer and the core of the relatively big tumors. We observed that Glc levels strikingly drop in the core of the big tumor, while other metabolites that can act as secondary carbon sources for tumors (lactate, glutamine, and serine) were all present at similar levels between core and the outer layer (Figure 7C). Moreover, when looking at the M+3 isotopologues of 3-PG, we observed that the ^{13}C enrichment is slightly higher on the outer layer than in the core (Figure 7D). In tumors, when the ^{13}C fraction of pyruvate is normalized to the ^{13}C fraction of 3-PG, the ratio is equal to one when newly synthesized pyruvate is entirely generated by glycolysis.[34] The ratio is in contrast >1 when other ^{13}C sources (also derived from the circulation) contribute to the pyruvate pool.[34] Comparing these ratios between the outer and inner layers of the B16-F10 tumors, we can see that the pyruvate ratio is ~2.3 in the inner core and 1.5 in the outer layer (Figure 7E). This indicates that the core is depleted of Glc in bigger tumors, and cells within this core are relying on additional carbon sources. In contrast, serine ratios remain rather constant, suggesting a switch of the glycolytic flux toward serine (Figure 7E). Even though these data are not definitive proof, they hint toward similar rewiring as observed *in vitro* when culturing cells in Gal instead of Glc.

In a second *in vivo* model, we performed the adoptive transfer of TCL1-355 into C57BL/6 mice as a model of chronic lymphocytic leukemia (CLL).[50,51] In this model, leukemic B cells proliferate rapidly within the spleen, which also resulted in decreased Glc concentration in the spleens of CLL mice compared to healthy mice (Figure 7F). Following [U-^{13}C]Glc infusion, we compared B cells from healthy spleens against CLL B cells from diseased spleens, and we observed that CLL cells significantly increased their relative flux from glucose toward serine and glycine while showing a reduced flux toward citrate (Figure 7G).

In summary, by using Gal, we are able to capture relevant metabolic features of tumor cells that occur in glucose-depleted TME, specifically, the glycolytic rewiring toward serine to support cancer cell metabolism. Interestingly, this switch appears to be controlled via a PKM2 block that depends on mitochondrial formate production.

DISCUSSION

In the present study, we discover a rewiring of glycolytic flux toward SSP via a PKM2 block when the glycolytic rate is limited. We were able to corroborate previously described rewiring of glutamine metabolism toward SSP under glucose starvation. By identifying the block of lower glycolysis at PKM2, we were able to add another mechanistic layer that describes a separation of the glutamine flux to either exclusively support SSP via PEPCK2 or TCA cycle via ME (Figure 5H). We observed that both fluxes contribute to the survival and proliferation of several cancer cell lines and to supply the 1C cycle with the necessary carbons to perform biosynthetic, bioenergetic, and redox balance functions.

Cancer cells *in vitro* usually engage in aerobic glycolysis due to the ample availability of glucose. This does not reflect glucose levels and cancer cell metabolism within the TME as demonstrated with analyses of the tumor interstitial fluid (TIF).[22,23] TIF measurements represent the average level of glucose across the area of the whole tumor. However, inside the tumor, areas do exist where cells are even more deprived of glucose (Figure 7C), and those cells withstanding such severe metabolic stress (alongside other niche stresses) are the plastic cells that are capable of surviving such stressful microenvironments.[15] Uncovering the metabolic rewiring in these deprived cells holds therapeutic promise to target cancer growth and metastasis.[25]

By culturing cancer cells under glycolytic stress conditions, we were able to see their ability to use the same carbon source for different functions upon the PKM2 block and rewiring of carbons toward SSP. On the other hand, cancer cells also engage on glutamine as an additional carbon source to support SSP, showcasing an example of metabolic flexibility.[14] It is intriguing that the mitochondrial isoform of PEPCK is involved under glycolytic limitations, as usually this isoform is only involved when cytoplasmic NADH levels are not depleted.[52] However, under glycolytic limitations, NAD/NADH ratio is increased, and yet, the cells still preferably engage PEPCK2 over cytoplasmic PEPCK1, whose involvement would transfer mitochondrial NADH to the cytoplasm via malate oxidation.[52] This finding can be explained by the possibility that the gluconeogenesis pathway is activated mainly to support SSP, and therefore, cytoplasmic NADH is not required to reduce 1,3-bisphosphoglycerate into glyceraldehyde 3-phosphate per the conventional gluconeogenesis pathway. Furthermore, an increased NAD/NADH ratio promotes PHGDH flux.[38] In contrast to previous reports, loss of PEPCK2 did not diminish proliferation

(D) Fractional enrichment from [U-^{13}C]galactose into M+2 citrate and M+3 serine after 24-h incubation (Gal+ 100 μM TEPP-46) as measured with LC-MS.
(E) 2D proliferation of MDA-MB-468 treated with 100 μM of TEPP-46 with either glucose or galactose and measured as cell counts at 72 h relative to proliferation under glucose.
(F) Relative intracellular levels of serine under galactose ± serine/glycine (SG) and treated with 15 μM PHGDHi. Relative levels are represented as peak areas (PAs) normalized to packed cell volume (PCV) in picoliters (pL) in MDA-MB-468 cells harboring PEPCK2 KD.
(G) Fractional enrichment from [U-^{13}C]galactose into M+2 citrate in MDA-MB-468 cells harboring PEPCK2 KD. (B–G) Each dot represents an independent experiment (from at least 3 different replicate wells). Mean ± SEM, *$p < 0.05$, **$p < 0.01$, ***$p < 0.001$, ****$p < 0.0001$, ns $p > 0.1$. p value is calculated by Student's t test, two-tailed, unpaired with Welch's correction.
(H) Schematic representation of the rewiring of glutamine metabolism that takes place under glycolytic limitation and the differentiation between ME and PEPCK2 fluxes.

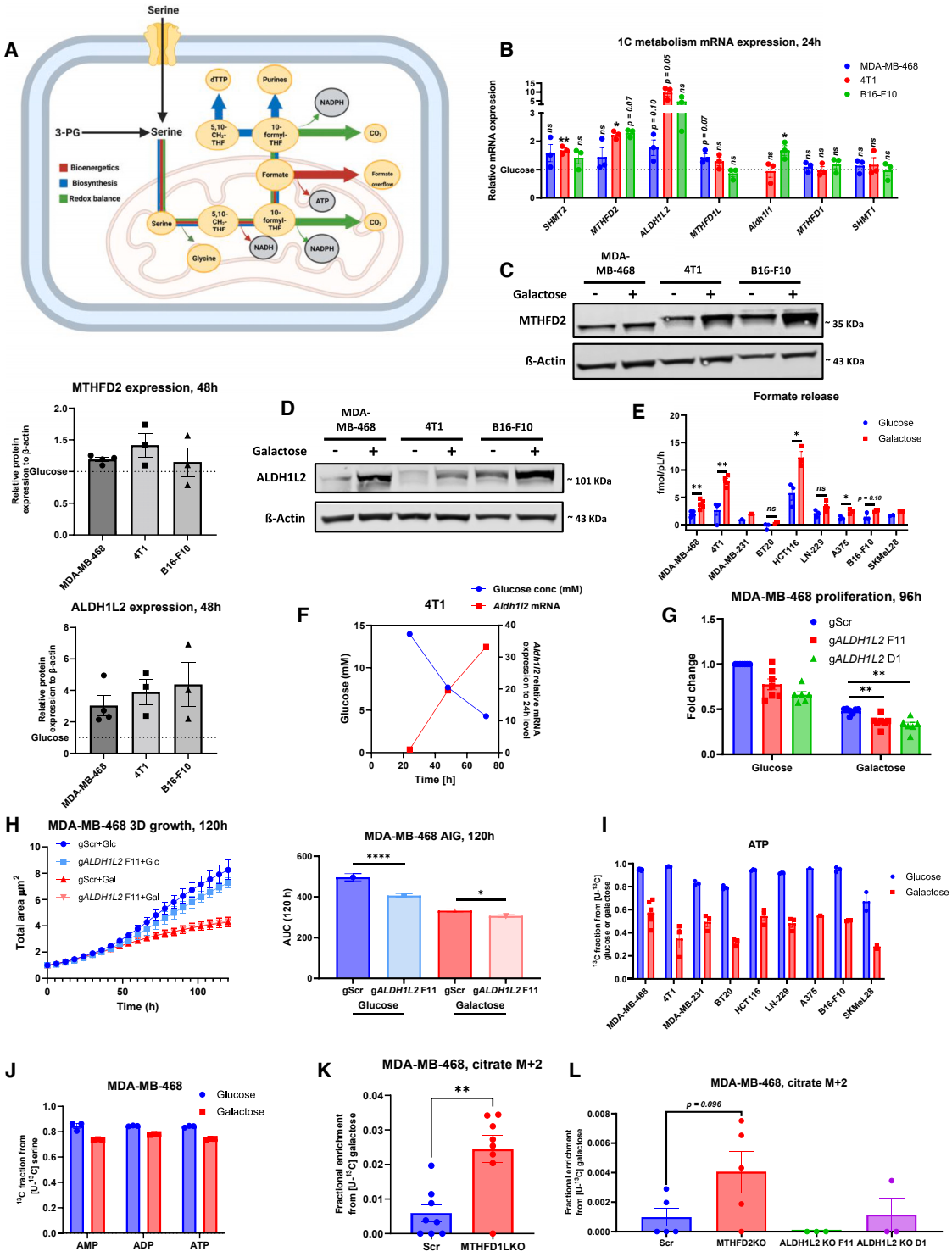

Figure 6. SSP flux is crucial to sustain mitochondrial formate production to support all three metabolic pillars

(A) Schematic representation of the one-carbon cycle with the different pillars and how it can contribute to biosynthesis and bioenergetic and redox balance.

(B) mRNA expression of *SHMT2*, *MTHFD2*, *ALDH1L2*, *MTHFD1L*, *Aldh1l1*, *MTHFD1*, and *SHMT1* genes relative to *GAPDH* and *ACTINβ* or *Gapdh and Sdha* after 24-h incubation with either glucose or galactose measured with qRT-PCR. Data are presented as fold change to the mRNA expression in cells cultured with glucose.

(C) Protein expression of MTHFD2 after 48-h incubation with either glucose or galactose, with the quantification of these signals relative to β-actin as a loading control and presented as a fold change of expression under galactose to that of glucose.

(legend continued on next page)

in our used models. One reason may root in the presence of galactose (compared to glucose starvation) and consequently a glycolytic (baseline) flux that can support serine synthesis as opposed to the complete lack of glycolysis during glucose starvation.

The diversion of the glycolytic flux away from lower glycolysis and toward SSP offers many metabolic advantages for the cell. For bioenergetics, SSP and the subsequent 1C cycle generate two NADH and one ATP per 3-PG molecule, while lower glycolysis generates one ATP and consumes one NADH. This means if energy is the main constraint for the cell under glycolytic limitation, it will benefit more from running SSP and the subsequent serine catabolism and formate overflow.[24] Furthermore, the additional advantage of sustaining the flux toward serine catabolism lies in its pathway flexibility. The fate of the 1C can be tailored for the cell's need; full oxidation of 1C via ALDH1L2 will generate NADPH, the MTHFD1L reaction will generate ATP, or it can be incorporated in purines and dTMP in the cytosol.[25] Here, we show that under glycolytic limitation, the rewiring toward SSP and 1C cycle supports all the three different pillars of metabolism, specifically the mitochondrial part of the 1C cycle (Figure 6). In fact, we observe that even though the cells increase the expression of ALDH1L2 and subsequently lose more carbon as CO_2, formate overflow is still increased, highlighting the non-biosynthetic benefit of running the mitochondrial branch of the 1C cycle under glycolytic limitation.

Cancer cells preferentially express PKM2 over other isozymes of pyruvate kinase as it provides them with the metabolic flexibility to regulate the glycolytic flux, as PKM2 can be regulated via allosteric signals that shift its form between a high-activity tetramer and a low-activity dimer.[41] This allows cancer cells to rewire their glycolytic flux toward biosynthetic pathways when needed by expressing the dimer form of PKM2 to accommodate higher proliferative rates.[41] In the present study, we observed a complete block of PKM2 activity when the glycolytic flux is limited to rewire the limited carbon input toward SSP. Previous work has shown that serine acts as an allosteric activator of PKM2, while the lack of extracellular serine leads to an inhibition of PKM2 activity.[45,53] Here, we observed that when glucose is limited, even with SG available in the media, PKM2 was inhibited. This indicates that even when serine was available for the cells, the lack of glycolytic carbons inhibited pyruvate kinase activity to rewire the glycolytic flux toward SSP. Moreover, when intracellular serine levels were diminished in our setup using SG starvation and PHGDH inhibition, we observed increased PKM2 activity as measured with M+2 citrate, indicating that the PKM2 inhibition we report is independent of serine levels. These observations highlight an intriguing difference between *de novo* serine synthesis flux and extracellular serine consumption and potentially could be explained by recent work that has shown that PHGDH functions beyond its catalytic activity within tumor cells and can allosterically regulate the function of phosphofructokinase.[54] Additionally, here we presented evidence that the removal of MTHFD2 or MTHFD1L was sufficient to partially re-establish PKM2 activity, meaning that mitochondrial 1C cycle is able to regulate PKM2 function alongside other regulators like FBP. This would hint at a possible link between the PKM2 block and the increased formate overflow under glycolytic limitation, especially since in the condition with no serine or formate overflow, PKM2 activity was increased (Figure 5G). Disentangling the direct cause of PKM2 block and the link with the 1C cycle is the subject of ongoing work in our lab.

The findings presented here highlight the flexibility and plasticity of the biochemical network in tumor cells. These adaptive traits present a challenge in developing precision-medicine drugs that target the cells' metabolism. For such therapeutic strategies to be successful, context-dependent understanding of environmental conditions and nutrient availability of the TME need to be considered alongside specific oncogenic driver mutations.[55]

Limitations of the study

In vivo, areas with limited glucose supply will arise due to the unorganized vasculature of solid tumors. However, such areas are quickly replenished with glucose from the circulation, and therefore, we speculate that cells in such areas are in constant glycolytic limitation status. Throughout the presented study, we have utilized galactose as a tool compound to mimic the glycolytic limitation that we hypothesize occurs within the TME. As with all models, such methodology is not the perfect imitation of what occurs within the TME. Modeling such a feature *in vitro* would require a system than constantly keeps glucose concentration low. While the present study pinpoints PKM2 as the main rewiring point between glycolysis and the TCA cycle, we were not able to fully elucidate the mechanism of PKM2 inhibition in the presented work. We have excluded current known mechanisms of PKM2 inhibition in this manuscript, and we also did not find evidence that nitric oxide may act as a regulator of PKM2 in our

(D) Protein expression of ALDH1L2 after 48-h incubation with either glucose or galactose, with the quantification of these signals relative to β-actin as a loading control and presented as a fold change of expression under galactose to that of glucose.
(E) Absolute quantification of formate release from the indicated cancer cell lines after 24-h incubation with either glucose or galactose.
(F) Concentration of glucose as measured in media in which 4T1 cells were cultured for 72 h, compared to *Aldh1l2* mRNA expression relative to *Gapdh* and presented as fold change for expression at 24 h. Data presented in (F) are from one independent experiment, and mRNA was extracted from single wells, while medium measurements are mean ± SEM of 3 different replicate wells.
(G) 2D proliferation of MDA-MB-468 Scramble and ALDH1L2KO cells cultured in either glucose or galactose as measured with cell counts at 96 h relative to proliferation of scramble cells under glucose.
(H) 3D growth of MDA-MB-468 control and ALDH1L2KO aggregates using anchorage-independent conditions in either glucose or galactose, with the corresponding AUC. 3 independent experiments are represented each with at least 6 different replicate wells.
(I) ^{13}C fraction in ATP from [U-^{13}C]glucose and galactose after 24-h incubation in multiple cell lines.
(J) ^{13}C fraction in AMP/ADP/ATP from [U-^{13}C]serine after 24-h incubation in MDA-MB-468.
(K and L) Fractional enrichment from [U-^{13}C]galactose into M+2 citrate after 24-h incubation in MDA-MB-468 Scramble compared to MTHFD1LKO (K) and MTHFD2KO and ALDH1L2KO (L) as measured with LC-MS. (B–L) Each dot represents an independent experiment averaged from 3 different replicate wells unless stated otherwise. Mean ± SEM, *$p < 0.05$, **$p < 0.01$, ***$p < 0.001$, ****$p < 0.0001$, ns $p > 0.1$. p value is calculated by Student's t test, two-tailed, unpaired with Welch's correction unless stated otherwise.

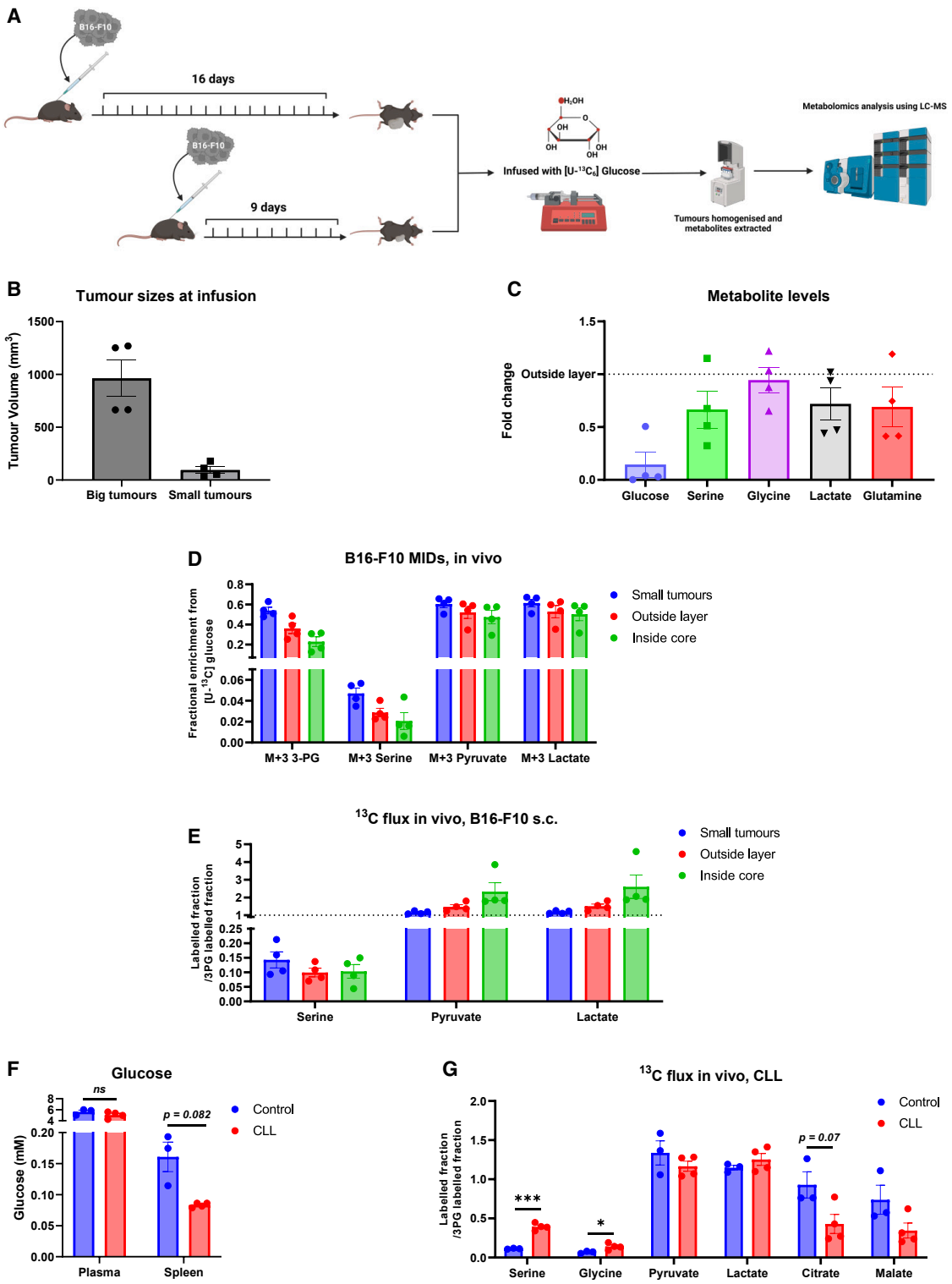

Figure 7. *In vivo* relevance of using Gal to model glycolytic limitation

(A) Schematic representation of the *in vivo* setup for B16-F10 subcutaneous tumors.

(B) Tumor volume of B16-F10 tumors grown subcutaneously on the flanks of C57BL/6 mice (n = 4/group).

(C) Metabolite levels measured from the inside core of B16-F10 tumors and presented as fold change of the level of those metabolites in the outside layer of the same tumors.

(legend continued on next page)

experimental setup. Elucidating the precise inhibition mechanism is still the subject of ongoing work in our lab.

While the *in vivo* models we have used in this manuscript partially recapitulate our *in vitro* findings, it cannot be concluded that the reported rewiring occurs within the TME. The reason being is that it was not possible to locate areas of glucose limitation in the tumor. Therefore, metabolites extracted from the tumor represented the average level over a certain area of the tumor. Identifying and profiling areas within the tumor that are limited in their glucose supply would be the next step to validate the observed rewiring *in vivo*.

STAR★METHODS

Detailed methods are provided in the online version of this paper and include the following:

- KEY RESOURCES TABLE
- RESOURCE AVAILABILITY
  - Lead contact
  - Materials availability
  - Data and code availability
- EXPERIMENTAL MODEL AND STUDY PARTICIPANT DETAILS
  - Cell lines culture
  - Animal experiments
  - TCL1-355 adoptive transfer
  - B16-F10 subcutaneous model
- METHOD DETAILS
  - Chemicals
  - Lentiviral mediated knockdown of *PCK2*
  - CRISPR/Cas9 KO of *Pck2, MTHFD2, ALDH1L2*
  - Western blot
  - Flow cytometry analysis
  - Proliferation assays
  - Anchorage independent 3D growth assays
  - RNA extraction, cDNA synthesis and RT-qPCR
  - Metabolomics
- QUANTIFICATION AND STATISTICAL ANALYSIS

SUPPLEMENTAL INFORMATION

Supplemental information can be found online at https://doi.org/10.1016/j.celrep.2024.113868.

ACKNOWLEDGMENTS

We are grateful to Stephanie Kreis (University of Luxembourg) for providing us with B16-F10, A375, and SKMeL28 cells; Clement Thomas (LIH, Luxembourg) for providing 4T1 and BT-20 cells; Lewis Cantley (Harvard Medical School) for providing MDA-MB-468 WT and MTHFD1LKO cells; and Dimitar Efremov (ICGEB, Trieste) for providing TCL1-355 cells. We are grateful for all the technical and analytical support from the different metabolomics platforms toward the work presented here and, in specific, Francois Bernardin from the metabolomics platform at LIH, and Xiangyi Dong, Floriane Gavotto, and Lucia Gallucci from the LCSB Metabolomics Platform (RRID:SCR 024769). We are thankful for the support of the National Cytometry Platform (Quantitative Biology Unit, LIH) for support with flow cytometry measurements and analysis. Figures 1A, 1B, 3K, 5A, 5H, 6A and 7A were created with BioRender.com.

M.B. is supported by the Fondation du Pélican de Mie et Pierre Hippert-Faber, under the aegis of the Fondation de Luxembourg. M.B. and J.M. are supported by the Luxembourg National Research Fund (FNR) ATTRACT program (A18/BM/11809970). M.B., J.M., and E.L. are supported by FNR-CORE grant (C21/BM/15718879/1cFlex). E.L. is supported by the FNR-CORE program (C16/BM/11282028 and C20/BM/14591557), by a Proof of Concept FNR grant (PoC/18/12554295), a PRIDE17/11823097, and by i2Tron (PRIDE19/14254520). E.G., J.P., and E.M. are supported by grants from the FNR and Fondation Cancer (PRIDE15/10675146/CANBIO, C20/BM/14582635, and C20/BM/14592342). E.V. is supported by FNRS-Télévie (7.4509.20 and 7.4572.22).

AUTHOR CONTRIBUTIONS

M.B. and J.M. conceptualized and designed the study. M.B., L.N., C.K., and B.B. performed all of the *in vitro* experiments. A.O., E.V., E.G., V.P., M.S., C.P., J.P., E.M., S.P.N., and E.L. assisted in the design and performing of the *in vivo* work. L.N., N.I.L., and M.W.R. aided in the generation of different KO cell lines used. D.S., M.W., C.J., and A.L. performed YSI, LC-MS, GC-MS, and IC-MS measurements, while M.B. performed the corresponding data analysis according to instructions from D.S., M.W., C.J., A.L., and J.M. Original draft was written by M.B. and J.M. Review and editing was done by all authors.

DECLARATION OF INTERESTS

The authors of the presented study declare no competing interests.

Received: June 8, 2023
Revised: December 14, 2023
Accepted: February 9, 2024
Published: February 28, 2024

REFERENCES

1. Crabtree, H.G. (1929). Observations on the carbohydrate metabolism of tumours. Biochem. J. *23*, 536–545. https://doi.org/10.1042/bj0230536.
2. Hanahan, D., and Weinberg, R.A. (2011). Hallmarks of cancer: the next generation. Cell *144*, 646–674. https://doi.org/10.1016/j.cell.2011.02.013.
3. Warburg, O. (1925). The Metabolism of Carcinoma Cells1. J. Cancer Res. *9*, 148–163. https://doi.org/10.1158/jcr.1925.148.
4. Vander Heiden, M.G., Cantley, L.C., and Thompson, C.B. (2009). Understanding the Warburg effect: the metabolic requirements of cell proliferation. Science *324*, 1029–1033. https://doi.org/10.1126/science.1160809.
5. Amendola, C.R., Mahaffey, J.P., Parker, S.J., Ahearn, I.M., Chen, W.C., Zhou, M., Court, H., Shi, J., Mendoza, S.L., Morten, M.J., et al. (2019). KRAS4A directly regulates hexokinase 1. Nature *576*, 482–486. https://doi.org/10.1038/s41586-019-1832-9.

(D) Fractional enrichment in tumor piece of the presented metabolites after 2-h infusion with [U-^{13}C]glucose via the tail vain.
(E) The ^{13}C flux from 3-PG toward multiple metabolites measured in B16-F10 tumors.
(F) Glucose concentration as measured in the plasma and in ground spleen tissue from control and CLL mice after 2 h of continuous infusion with [U-^{13}C]glucose. The concentration was determined using standard addition method.
(G) The ^{13}C flux from 3-PG toward multiple metabolites measured in CLL cells collected from the spleen of CLL mice. (B–G) Each dot represents a biological replicate. (A–F) Mean ± SEM, *p < 0.05, **p < 0.01, ***p < 0.001, ****p < 0.0001, ns p > 0.1. p value is calculated by Student's t test, two-tailed, unpaired with Welch's correction unless stated otherwise.

6. Fernandez-de-Cossio-Diaz, J., and Vazquez, A. (2017). Limits of aerobic metabolism in cancer cells. Sci. Rep. *7*, 13488. https://doi.org/10.1038/s41598-017-14071-y.

7. Locasale, J.W., Grassian, A.R., Melman, T., Lyssiotis, C.A., Mattaini, K.R., Bass, A.J., Heffron, G., Metallo, C.M., Muranen, T., Sharfi, H., et al. (2011). Phosphoglycerate dehydrogenase diverts glycolytic flux and contributes to oncogenesis. Nat. Genet. *43*, 869–874. https://doi.org/10.1038/ng.890.

8. Osthus, R.C., Shim, H., Kim, S., Li, Q., Reddy, R., Mukherjee, M., Xu, Y., Wonsey, D., Lee, L.A., and Dang, C.V. (2000). Deregulation of glucose transporter 1 and glycolytic gene expression by c-Myc. J. Biol. Chem. *275*, 21797–21800. https://doi.org/10.1074/jbc.C000023200.

9. Vazquez, A., Liu, J., Zhou, Y., and Oltvai, Z.N. (2010). Catabolic efficiency of aerobic glycolysis: The Warburg effect revisited. BMC Syst. Biol. *4*, 58. https://doi.org/10.1186/1752-0509-4-58.

10. Ying, H., Kimmelman, A.C., Lyssiotis, C.A., Hua, S., Chu, G.C., Fletcher-Sananikone, E., Locasale, J.W., Son, J., Zhang, H., Coloff, J.L., et al. (2012). Oncogenic Kras maintains pancreatic tumors through regulation of anabolic glucose metabolism. Cell *149*, 656–670. https://doi.org/10.1016/j.cell.2012.01.058.

11. de Alteriis, E., Cartenì, F., Parascandola, P., Serpa, J., and Mazzoleni, S. (2018). Revisiting the Crabtree/Warburg effect in a dynamic perspective: a fitness advantage against sugar-induced cell death. Cell Cycle *17*, 688–701. https://doi.org/10.1080/15384101.2018.1442622.

12. Luengo, A., Li, Z., Gui, D.Y., Sullivan, L.B., Zagorulya, M., Do, B.T., Ferreira, R., Naamati, A., Ali, A., Lewis, C.A., et al. (2021). Increased demand for NAD(+) relative to ATP drives aerobic glycolysis. Mol. Cell *81*, 691–707.e6. https://doi.org/10.1016/j.molcel.2020.12.012.

13. Wang, Y., Stancliffe, E., Fowle-Grider, R., Wang, R., Wang, C., Schwaiger-Haber, M., Shriver, L.P., and Patti, G.J. (2022). Saturation of the mitochondrial NADH shuttles drives aerobic glycolysis in proliferating cells. Mol. Cell *82*, 3270–3283.e9. https://doi.org/10.1016/j.molcel.2022.07.007.

14. Bergers, G., and Fendt, S.M. (2021). The metabolism of cancer cells during metastasis. Nat. Rev. Cancer *21*, 162–180. https://doi.org/10.1038/s41568-020-00320-2.

15. Fendt, S.-M., Frezza, C., and Erez, A. (2020). Targeting Metabolic Plasticity and Flexibility Dynamics for Cancer Therapy. Cancer Discov. *10*, 1797–1807. https://doi.org/10.1158/2159-8290.Cd-20-0844.

16. Cantor, J.R. (2019). The Rise of Physiologic Media. Trends Cell Biol. *29*, 854–861. https://doi.org/10.1016/j.tcb.2019.08.009.

17. Díaz-Ruiz, R., Avéret, N., Araiza, D., Pinson, B., Uribe-Carvajal, S., Devin, A., and Rigoulet, M. (2008). Mitochondrial oxidative phosphorylation is regulated by fructose 1,6-bisphosphate. A possible role in Crabtree effect induction? J. Biol. Chem. *283*, 26948–26955. https://doi.org/10.1074/jbc.M800408200.

18. Holden, H.M., Rayment, I., and Thoden, J.B. (2003). Structure and function of enzymes of the Leloir pathway for galactose metabolism. J. Biol. Chem. *278*, 43885–43888. https://doi.org/10.1074/jbc.R300025200.

19. Rempel, A., Mathupala, S.P., Griffin, C.A., Hawkins, A.L., and Pedersen, P.L. (1996). Glucose catabolism in cancer cells: amplification of the gene encoding type II hexokinase. Cancer Res. *56*, 2468–2471.

20. Wilson, J.E. (2003). Isozymes of mammalian hexokinase: structure, subcellular localization and metabolic function. J. Exp. Biol. *206*, 2049–2057. https://doi.org/10.1242/jeb.00241.

21. Timson, D.J., and Reece, R.J. (2003). Functional analysis of disease-causing mutations in human galactokinase. Eur. J. Biochem. *270*, 1767–1774. https://doi.org/10.1046/j.1432-1033.2003.03538.x.

22. Sullivan, M.R., Danai, L.V., Lewis, C.A., Chan, S.H., Gui, D.Y., Kunchok, T., Dennstedt, E.A., Vander Heiden, M.G., and Muir, A. (2019). Quantification of microenvironmental metabolites in murine cancers reveals determinants of tumor nutrient availability. Elife *8*, e44235. https://doi.org/10.7554/eLife.44235.

23. Reinfeld, B.I., Madden, M.Z., Wolf, M.M., Chytil, A., Bader, J.E., Patterson, A.R., Sugiura, A., Cohen, A.S., Ali, A., Do, B.T., et al. (2021). Cell-programmed nutrient partitioning in the tumour microenvironment. Nature *593*, 282–288. https://doi.org/10.1038/s41586-021-03442-1.

24. Meiser, J., Tumanov, S., Maddocks, O., Labuschagne, C.F., Athineos, D., Van Den Broek, N., Mackay, G.M., Gottlieb, E., Blyth, K., Vousden, K., et al. (2016). Serine one-carbon catabolism with formate overflow. Sci. Adv. *2*, e1601273. https://doi.org/10.1126/sciadv.1601273.

25. Benzarti, M., Delbrouck, C., Neises, L., Kiweler, N., and Meiser, J. (2020). Metabolic Potential of Cancer Cells in Context of the Metastatic Cascade. Cells *9*. https://doi.org/10.3390/cells9092035.

26. Kiweler, N., Delbrouck, C., Pozdeev, V.I., Neises, L., Soriano-Baguet, L., Eiden, K., Xian, F., Benzarti, M., Haase, L., Koncina, E., et al. (2022). Mitochondria preserve an autarkic one-carbon cycle to confer growth-independent cancer cell migration and metastasis. Nat. Commun. *13*, 2699. https://doi.org/10.1038/s41467-022-30363-y.

27. Hyroššová, P., Aragó, M., Moreno-Felici, J., Fu, X., Mendez-Lucas, A., García-Rovés, P.M., Burgess, S., Figueras, A., Viñals, F., and Perales, J.C. (2021). PEPCK-M recoups tumor cell anabolic potential in a PKC-ζ-dependent manner. Cancer Metabol. *9*, 1. https://doi.org/10.1186/s40170-020-00236-3.

28. Keshet, R., Lee, J.S., Adler, L., Iraqi, M., Ariav, Y., Lim, L.Q.J., Lerner, S., Rabinovich, S., Oren, R., Katzir, R., et al. (2020). Targeting purine synthesis in ASS1-expressing tumors enhances the response to immune checkpoint inhibitors. Nat. Can. (Ott.) *1*, 894–908. https://doi.org/10.1038/s43018-020-0106-7.

29. Leithner, K., Hrzenjak, A., Trötzmüller, M., Moustafa, T., Köfeler, H.C., Wohlkoenig, C., Stacher, E., Lindenmann, J., Harris, A.L., Olschewski, A., and Olschewski, H. (2015). PCK2 activation mediates an adaptive response to glucose depletion in lung cancer. Oncogene *34*, 1044–1050. https://doi.org/10.1038/onc.2014.47.

30. Vincent, E.E., Sergushichev, A., Griss, T., Gingras, M.C., Samborska, B., Ntimbane, T., Coelho, P.P., Blagih, J., Raissi, T.C., Choinière, L., et al. (2015). Mitochondrial Phosphoenolpyruvate Carboxykinase Regulates Metabolic Adaptation and Enables Glucose-Independent Tumor Growth. Mol. Cell *60*, 195–207. https://doi.org/10.1016/j.molcel.2015.08.013.

31. Yang, C., Ko, B., Hensley, C.T., Jiang, L., Wasti, A.T., Kim, J., Sudderth, J., Calvaruso, M.A., Lumata, L., Mitsche, M., et al. (2014). Glutamine oxidation maintains the TCA cycle and cell survival during impaired mitochondrial pyruvate transport. Mol. Cell *56*, 414–424. https://doi.org/10.1016/j.molcel.2014.09.025.

32. Lyssiotis, C.A., and Kimmelman, A.C. (2017). Metabolic Interactions in the Tumor Microenvironment. Trends Cell Biol. *27*, 863–875. https://doi.org/10.1016/j.tcb.2017.06.003.

33. Hui, S., Ghergurovich, J.M., Morscher, R.J., Jang, C., Teng, X., Lu, W., Esparza, L.A., Reya, T., Le, Z., Yanxiang Guo, J., et al. (2017). Glucose feeds the TCA cycle via circulating lactate. Nature *551*, 115–118. https://doi.org/10.1038/nature24057.

34. Faubert, B., Li, K.Y., Cai, L., Hensley, C.T., Kim, J., Zacharias, L.G., Yang, C., Do, Q.N., Doucette, S., Burguete, D., et al. (2017). Lactate Metabolism in Human Lung Tumors. Cell *171*, 358–371.e9. https://doi.org/10.1016/j.cell.2017.09.019.

35. Cheung, S.M., Husain, E., Masannat, Y., Miller, I.D., Wahle, K., Heys, S.D., and He, J. (2020). Lactate concentration in breast cancer using advanced magnetic resonance spectroscopy. Br. J. Cancer *123*, 261–267. https://doi.org/10.1038/s41416-020-0886-7.

36. Leithner, K., Triebl, A., Trötzmüller, M., Hinteregger, B., Leko, P., Wieser, B.I., Grasmann, G., Bertsch, A.L., Züllig, T., Stacher, E., et al. (2018). The glycerol backbone of phospholipids derives from noncarbohydrate precursors in starved lung cancer cells. Proc. Natl. Acad. Sci. USA *115*, 6225–6230. https://doi.org/10.1073/pnas.1719871115.

37. Vande Voorde, J., Ackermann, T., Pfetzer, N., Sumpton, D., Mackay, G., Kalna, G., Nixon, C., Blyth, K., Gottlieb, E., and Tardito, S. (2019). Improving the metabolic fidelity of cancer models with a physiological cell culture medium. Sci. Adv. *5*, eaau7314. https://doi.org/10.1126/sciadv.aau7314.

38. Diehl, F.F., Lewis, C.A., Fiske, B.P., and Vander Heiden, M.G. (2019). Cellular redox state constrains serine synthesis and nucleotide production to impact cell proliferation. Nat. Metab. *1*, 861–867. https://doi.org/10.1038/s42255-019-0108-x.

39. Lemaigre, F.P., and Rousseau, G.G. (1994). Transcriptional control of genes that regulate glycolysis and gluconeogenesis in adult liver. Biochem. J. *303*, 1–14. https://doi.org/10.1042/bj3030001.

40. Anastasiou, D., Yu, Y., Israelsen, W.J., Jiang, J.K., Boxer, M.B., Hong, B.S., Tempel, W., Dimov, S., Shen, M., Jha, A., et al. (2012). Pyruvate kinase M2 activators promote tetramer formation and suppress tumorigenesis. Nat. Chem. Biol. *8*, 839–847. https://doi.org/10.1038/nchembio.1060.

41. Dayton, T.L., Jacks, T., and Vander Heiden, M.G. (2016). PKM2, cancer metabolism, and the road ahead. EMBO Rep. *17*, 1721–1730. https://doi.org/10.15252/embr.201643300.

42. Dombrauckas, J.D., Santarsiero, B.D., and Mesecar, A.D. (2005). Structural basis for tumor pyruvate kinase M2 allosteric regulation and catalysis. Biochemistry *44*, 9417–9429. https://doi.org/10.1021/bi0474923.

43. Bond, C.J., Jurica, M.S., Mesecar, A., and Stoddard, B.L. (2000). Determinants of allosteric activation of yeast pyruvate kinase and identification of novel effectors using computational screening. Biochemistry *39*, 15333–15343. https://doi.org/10.1021/bi001443i.

44. Anastasiou, D., Poulogiannis, G., Asara, J.M., Boxer, M.B., Jiang, J.K., Shen, M., Bellinger, G., Sasaki, A.T., Locasale, J.W., Auld, D.S., et al. (2011). Inhibition of pyruvate kinase M2 by reactive oxygen species contributes to cellular antioxidant responses. Science *334*, 1278–1283. https://doi.org/10.1126/science.1211485.

45. Chaneton, B., Hillmann, P., Zheng, L., Martin, A.C.L., Maddocks, O.D.K., Chokkathukalam, A., Coyle, J.E., Jankevics, A., Holding, F.P., Vousden, K.H., et al. (2012). Serine is a natural ligand and allosteric activator of pyruvate kinase M2. Nature *491*, 458–462. https://doi.org/10.1038/nature11540.

46. Weinstabl, H., Treu, M., Rinnenthal, J., Zahn, S.K., Ettmayer, P., Bader, G., Dahmann, G., Kessler, D., Rumpel, K., Mischerikow, N., et al. (2019). Intracellular Trapping of the Selective Phosphoglycerate Dehydrogenase (PHGDH) Inhibitor BI-4924 Disrupts Serine Biosynthesis. J. Med. Chem. *62*, 7976–7997. https://doi.org/10.1021/acs.jmedchem.9b00718.

47. Smith, G.K., Banks, S.D., Monaco, T.J., Rigual, R., Duch, D.S., Mullin, R.J., and Huber, B.E. (1990). Activity of an NAD-dependent 5,10-methylenetetrahydrofolate dehydrogenase in normal tissue, neoplastic cells, and oncogene-transformed cells. Arch. Biochem. Biophys. *283*, 367–371. https://doi.org/10.1016/0003-9861(90)90656-j.

48. Lorenz, N.I., Sauer, B., Zeiner, P.S., Strecker, M.I., Luger, A.-L., Schulte, D., Mittelbronn, M., Alekseeva, T., Sevenich, L., Harter, P.N., et al. (2022). AMP-kinase mediates adaptation of glioblastoma cells to conditions of the tumour microenvironment. Preprint at bioRxiv. https://doi.org/10.1101/2022.03.25.485624.

49. Fan, J., Ye, J., Kamphorst, J.J., Shlomi, T., Thompson, C.B., and Rabinowitz, J.D. (2014). Quantitative flux analysis reveals folate-dependent NADPH production. Nature *510*, 298–302. https://doi.org/10.1038/nature13236.

50. Bichi, R., Shinton, S.A., Martin, E.S., Koval, A., Calin, G.A., Cesari, R., Russo, G., Hardy, R.R., and Croce, C.M. (2002). Human chronic lymphocytic leukemia modeled in mouse by targeted TCL1 expression. Proc. Natl. Acad. Sci. USA *99*, 6955–6960. https://doi.org/10.1073/pnas.102181599.

51. Chakraborty, S., Martines, C., Porro, F., Fortunati, I., Bonato, A., Dimishkovska, M., Piazza, S., Yadav, B.S., Innocenti, I., Fazio, R., et al. (2021). B-cell receptor signaling and genetic lesions in TP53 and CDKN2A/CDKN2B cooperate in Richter transformation. Blood *138*, 1053–1066. https://doi.org/10.1182/blood.2020008276.

52. Nelson, D.L.a. (2017). Lehninger Principles of Biochemistry (Macmillan Higher Education).

53. Ye, J., Mancuso, A., Tong, X., Ward, P.S., Fan, J., Rabinowitz, J.D., and Thompson, C.B. (2012). Pyruvate kinase M2 promotes de novo serine synthesis to sustain mTORC1 activity and cell proliferation. Proc. Natl. Acad. Sci. USA *109*, 6904–6909. https://doi.org/10.1073/pnas.1204176109.

54. Rossi, M., Altea-Manzano, P., Demicco, M., Doglioni, G., Bornes, L., Fukano, M., Vandekeere, A., Cuadros, A.M., Fernández-García, J., Riera-Domingo, C., et al. (2022). PHGDH heterogeneity potentiates cancer cell dissemination and metastasis. Nature *605*, 747–753. https://doi.org/10.1038/s41586-022-04758-2.

55. Muir, A., and Vander Heiden, M.G. (2018). The nutrient environment affects therapy. Science *360*, 962–963. https://doi.org/10.1126/science.aar5986.

56. Zheng, Y., Lin, T.Y., Lee, G., Paddock, M.N., Momb, J., Cheng, Z., Li, Q., Fei, D.L., Stein, B.D., Ramsamooj, S., et al. (2018). Mitochondrial One-Carbon Pathway Supports Cytosolic Folate Integrity in Cancer Cells. Cell *175*, 1546–1560.e17. https://doi.org/10.1016/j.cell.2018.09.041.

57. Hiller, K., Hangebrauk, J., Jäger, C., Spura, J., Schreiber, K., and Schomburg, D. (2009). MetaboliteDetector: comprehensive analysis tool for targeted and nontargeted GC/MS based metabolome analysis. Anal. Chem. *81*, 3429–3439. https://doi.org/10.1021/ac802689c.

58. Rattigan, K.M., Brabcova, Z., Sarnello, D., Zarou, M.M., Roy, K., Kwan, R., de Beauchamp, L., Dawson, A., Ianniciello, A., Khalaf, A., et al. (2023). Pyruvate anaplerosis is a targetable vulnerability in persistent leukaemic stem cells. Nat. Commun. *14*, 4634. https://doi.org/10.1038/s41467-023-40222-z.

59. Wang, T., Gnanaprakasam, J.N.R., Chen, X., Kang, S., Xu, X., Sun, H., Liu, L., Rodgers, H., Miller, E., Cassel, T.A., et al. (2020). Inosine is an alternative carbon source for CD8(+)-T-cell function under glucose restriction. Nat. Metab. *2*, 635–647. https://doi.org/10.1038/s42255-020-0219-4.

60. Dranka, B.P., Benavides, G.A., Diers, A.R., Giordano, S., Zelickson, B.R., Reily, C., Zou, L., Chatham, J.C., Hill, B.G., Zhang, J., et al. (2011). Assessing bioenergetic function in response to oxidative stress by metabolic profiling. Free Radic. Biol. Med. *51*, 1621–1635. https://doi.org/10.1016/j.freeradbiomed.2011.08.005.

STAR★METHODS

KEY RESOURCES TABLE

REAGENT or RESOURCE	SOURCE	IDENTIFIER
Antibodies		
AMPKα	Cell Signaling Technology	5831T; RRID: AB_10622186
p-AMPK^{Thr172}	Cell Signaling Technology	2535; RRID:AB_331250
ACC	Cell Signaling Technology	3676S; RRID:AB_2219397
p-ACC^{Ser79}	Cell Signaling Technology	11818S; RRID: AB_2687505
MTHFD2	Cell Signaling Technology	41377S; RRID:AB_2799200
ALDH1L2	Sigma Aldrich Proteintech	HPA039481; RRID:AB_10795465 21391-1-AP; RRID:AB_2878854
PSAT1	Sigma Aldrich	HPA042924; RRID: AB_2678223
PSPH	Sigma Aldrich	HPA020376; RRID:AB_1855867
PHGDH	Sigma Aldrich	HPA021241; RRID:AB_1855299
PEPCK2	Cell Signaling Technology	6924S; RRID:AB_10836185
MTHFD1L	Proteintech	16113-1-AP; RRID:AB_2250974
β-Actin	Cell Signaling Technology	3700; RRID:AB_2242334
mCD5-PE clone: 53–7.3	Biolegend	100608; RRID:AB_312737
mCD19-PE/Vio770 clone: 6D5	Miltenyi	130-102-361; RRID:AB_2661118
AnnexinV-FITC	ImmunoTools GmbH	31490013
IRDye 680RD Goat Anti-Mouse IgG (H + L)	LI-COR	925–68070 Lot# C80619-01
IRDye 800CW Donkey Anti-Rabbit IgG (H + L)	LI-COR	925–32213 Lot# C80829-10
Chemicals, peptides, and recombinant proteins		
[U-^{13}C]D-glucose	Cambridge Isotope Laboratories	CLM-1396
[U-^{13}C]D-galactose	Cambridge Isotope Laboratories	CLM-1570
[U-^{13}C]L-glutamine	Cambridge Isotope Laboratories	CLM-1822
[U-^{13}C]sodium L-lactate	Sigma Aldrich	485926
[U-^{13}C]L-serine	Cambridge Isotope Laboratories	CLM-1574
[U-^{13}C]Palmitic acid	Cambridge Isotope Laboratories	CLM-409
[^{15}N-amine] L-glutamine	Cambridge Isotope Laboratories	NLM-1016
Canonical Amino Acid Mix	Cambridge Isotope Laboratories	MSK-CAA-1
D-(+)-Galactose	Sigma Aldrich	G0750-25G
D-Glucose 45% solution in H_2O	Sigma Aldrich	G8769-100ML
L-Serine	Sigma Aldrich	84959
Glycine	Sigma Aldrich	50046
Sodium L-lactate	Sigma Aldrich	71718
L-Glutamine solution, 200 mM in H_2O	Sigma Aldrich	G7513-100ML
TEPP-46	MedChemExpress	HY-18657
BI-4916	MedChemExpress	HY-126253
Sodium chloride	Carl Roth	HN00.2
EDTA	Sigma Aldrich	ED-100G
NP-40	BioChemika	56741
cOmplete™, Mini Protease Inhibitor Cocktail	Sigma Aldrich	4693124001
PhosSTOP	Sigma Aldrich	4906837001

(*Continued on next page*)

Continued

REAGENT or RESOURCE	SOURCE	IDENTIFIER
SurePAGE™, Bis-Tris, 10x8, 4–12%, 12 wells	GeneScript	M00653
NuPAGE™ LDS Sample Buffer	Thermo Fisher Scientific	NP0007
Bovine Serum Albumin (BSA) Fraction V, fatty acid-free	Carl Roth	9638.3
Lipofectamine 3000	Thermo Fisher Scientific	L3000008
Methanol ROTISOLV® ≥99,9%, GC Ultra Grade	Carl Roth	KK44.1
Acetonitrile ROTISOLV® ≥99,95%, LC-MS Grade	Carl Roth	AE70.1
DMEM	Thermo Fisher Scientific	A1443001
RPMI1640	Thermo Fisher Scientific	61870010
Advanced DMEM/F12	Thermo Fisher Scientific	12634010
RPMI 1640 for SILAC	Thermo Fisher Scientific	88365
Advanced DMEM/F12 for SILAC	Thermo Fisher Scientific	A2494301
Customized DMEM powder lacking: glucose, pyruvate, glutamine, serine, glycine, tryptophan, phenol red and sodium bicarbonate.	Thermo Fisher Scientific	lot No. GME11933004
Fetal Bovine Serum, dialyzed, US origin, One Shot™ format	Thermo Fisher Scientific	26400044
FBS - charcoal stripped	Sigma Aldrich	F6765
H_2DCFDA	Thermo Fisher Scientific	D399
N-acetylcysteine (NAC)	Sigma Aldrich	A9166
Critical commercial assays		
RNeasy Mini Kit	Qiagen	74104
High Capacity cDNA Reverse Transcription Kit	Thermo Fisher Scientific	4368814
Fast SYBR™ Green Master Mix	Thermo Fisher Scientific	4368814
MojoSort™ Mouse Pan B Cell Isolation Kit II	BioLegend	480088
Experimental models: Organism/strains		
C57BL/6	Janvier's lab (France)	N/A
Experimental models: Cell lines		
MDA-MB-468	Lewis Cantley lab, Weill Cornell Medical College, USA. Originally from ATCC	HTB-132 Zheng et al, [56]
MDA-MB-468 MTHFD1LKO	Lewis Cantley lab, Weill Cornell Medical College, USA	Zheng et al, [56]
4T1	Clement Thomas lab, Luxembourg institute of Health, Luxembourg	N/A
B16-F10	Stephanie Kreis lab, University of Luxembourg, Luxembourg	N/A
MDA-MB-231	Alexei Vasquez lab, Beatson Institute of Cancer Research, UK	N/A
HCT116	Elisabeth LETELLIER lab, University of Luxembourg, Luxembourg.	N/A
LN-229	Simone Niclou lab, Luxembourg institute of Health, Luxembourg	N/A
LN-229 AMPK-dKO	Michael Ronellenfitsch lab, Dr Senckenberg Institute of Neurooncology, University Hospital Frankfurt, Goethe University	Lorenz.et al, [48]

(*Continued on next page*)

Continued

REAGENT or RESOURCE	SOURCE	IDENTIFIER
A375	Stephanie Kreis lab, University of Luxembourg, Luxembourg	N/A
SKMeL28	Stephanie Kreis lab, University of Luxembourg, Luxembourg	N/A
BT20	Clement Thomas lab, Luxembourg institute of Health, Luxembourg	N/A
TCL1-355	Dimitar Efremov lab, International Center for Genetic Engineering and Biotechnology, Trieste, Italy.	Chakraborty et al, [51]
Oligonucleotides		
Psph Fw: 5′- AGATTTCCCAGGGATCCGGC -3′ *Psph* Rv: 5′- CAGTCCTCACTCAAGGCTCG -3′	Eurogentec	N/A
Psat1 Fw: 5′- CCCAGCTGTGCGGAATGAGA -3′ *Psat1* Rv: 5′- GAGCACACTGATGCCGAGTC -3′	Eurogentec	N/A
Phgdh Fw: 5′- CAGTGCAAGAAAGGTGTGCG -3′ *Phgdh* Rv: 5′- TTCTCGTGGTCCACTAAGGC -3′	Eurogentec	N/A
Shmt1 Fw: 5′- TGCCCTCCCCATTTGAACAC -3′ *Shmt1* Rv: 5′-ATCTCTTTGCCAGTCTTGGGAT-3′	Eurogentec	N/A
Shmt2 Fw: 5′- CTGCACAGTGGGGAGTCAAT -3′ *Shmt2* Rv: 5′- GTCAGTGCCAGGTTGAGCTT -3′	Eurogentec	N/A
Mthfd2 Fw: 5′- CTGCGTTGGCTGTGCGGTT -3′ *Mthfd2* Rv: 5′- CTGAGGTGTGGCCGCTTGT -3′	Eurogentec	N/A
Mthfd1 Fw: 5′- CGTGGGTGGCAGACTAGCAA -3′ *Mthfd1* Rv: 5′- TACCTGCTCCTGCATCCGAG -3′	Eurogentec	N/A
Aldh1l1 Fw: 5′- TAGCAGGTGCCTTCCAACCT -3′ *Aldh1l1* Rv: 5′- CTTAAACACGGGCACGCCAT -3′	Eurogentec	N/A
Aldh1l2 Fw: 5′- TTGACAGCCCAAAGCATGGC -3′ *Aldh1l2* Rv:5′-CTGCCCAGAAAACAGAAAACCCA-3′	Eurogentec	N/A
Mthfd1l Fw: 5′- CTTTGGTGGGAACGATGAGCA -3′ *Mthfd1l* Rv: 5′- CCAGCCTTGACCGCATCTT -3′	Eurogentec	N/A
Gapdh Fw: 5′-CATCACTGCCACCCAGAAGACTG -3′ *Gapdh* Rv: 5′- ATGCCAGTGAGCTTCCCGTTCAG -3′	Eurogentec	N/A
Sdha Fw: 5′- CTTCGCTGGTGTGGATGTCA -3′ *Sdha* Rv: 5′- GTGGGAATCCCACCCATGT -3′	Eurogentec	N/A
PSPH Fw: 5′- GACAGCACGGTCATCAGAGAAG -3′ *PSPH* Rv: 5′- CGCTCTGTGAGAGCAGCTTTGA -3′	Eurogentec	N/A
PSAT1 Fw: 5′- GGCTTGGTTCTGGAGTGGAT -3′ *PSAT1* Rv: 5′- ATGCCTCCCACAGACACGTA -3′	Eurogentec	N/A
PHGDH Fw: 5′- CTTACCAGTGCCTTCTCTCCAC -3′ *PHGDH* Rv: 5′- GCTTAGGCAGTTCCCAGCATTC -3′	Eurogentec	N/A
SHMT1 Fw: 5′- GAAGAAAATCTCTGCCACGTCC -3′ *SHMT1* Rv: 5′- GATCAGCTTCGGGTGGAAGAG -3′	Eurogentec	N/A
SHMT2 Fw:5′-GCCTCATTGACTACAACCAGCTG-3′ *SHMT2* Rv: 5′- ATGTCTGCCAGCAGGTGTGCTT -3′	Eurogentec	N/A
MTHFD1 Fw:5′-TTGGACAGGCTCCAACGGAGAA-3′ *MTHFD1* Rv:5′-AGAAGTGGTGAGAGCCAGGACA-3′	Eurogentec	N/A
MTHFD2 Fw:5′-CTCCTTGTTCAGTTGCCTCTTCC-3′ *MTHFD2* Rv:5′-CTGATCCAAACACATTCGTCCTAC-3′	Eurogentec	N/A
MTHFD1L Fw: 5′- CGCACACCTGAATGTCAACTCC -3′ *MTHFD1L* Rv: 5′- CGTGGATGTCTCCAGTCAAGTG -3′	Eurogentec	N/A
ALDH1L2 Fw: 5′- CTTCTCCACTGGCCGGGTTTAT -3′ *ALDH1L2* Rv: 5′- CTGGAACTGTGAACACCCCT -3′	Eurogentec	N/A

(*Continued on next page*)

Continued

REAGENT or RESOURCE	SOURCE	IDENTIFIER
GAPDH Fw: 5′- CATGAGAAGTATGACAACAGCCT -3′ *GAPDH* Rv: 5′- AGTCCTTCCACGATACCAAAGT -3′	Eurogentec	N/A
ACTINβ Fw: 5′- CACCCTGAAGTACCCCATCG -3′ *ACTINβ* Rv: 5′- GCTGGGGTGTTGAAGGTCTC -3′	Eurogentec	N/A
pGIPZ-shSCR: TTACTCTCGCCCAAGCGAG	Horizon Discovery	RHS4346
pGIPZ sh*PCK2*-2: ATTATTGGACAGTCTTTGT	Horizon Discovery	RHS4430-200271196 V3LHS_410309
pGIPZ sh*ALDH1L2*: ACTGCTTTATCAACATCCG	Horizon Discovery	V3LHS_385780
scramble_gRNA: GTGTAGTTCGACCATTCGTG	Vector Builder	VB190718-1103vja
g*Pck2*: TATGCGTATTATGACCCGCC	Vector Builder	VB211125-1122kdb, gRNA #654
g*Pck2*: GCGGGTCATAATACGCATAC	Vector Builder	VB211125-1123gfv, gRNA #653
g*ALDH1L2*: GCAGAAGCCTACAGATCCGT	Vector Builder	VB190719-1044jbf, gRNA #1529
g*ALDH1L2*: GCGCTCCGGCGCTTCTCCAC	Vector Builder	VB190719-1054khg, gRNA #1st Exon
g*MTHFD2:* CGCCAACCAGGATCACACTC	Vector Builder	VB190718-1104ncn gRNA #918
gScramble: GTGTAGTTCGACCATTCGTG	Vector Builder	VB190718-1103vja gRNA 1
Software and algorithms		
MetaboliteDetector software		Hiller et al, [57] version 3.220180913
Seahorse Wave Desktop software	Agilent	Version 2.6.0
GraphPad PRISM software	GraphPad	Version 9.5.0
Incucyte S3 software	Sartorius	Version 2022
QuantStudio Design and Analysis software	Applied Biosciences, ThermoFisher Scientific	Version 1.5.1
Image StudioLite software	Li-COR	Version 5.2.
NovoExpress	Agilent	Version 1.5.0.
Flowjo software	BD Biosciences	Version 10.6.2.
Thermo Xcalibur software software	Thermo Fisher Scientific	Version 4.3.73.11
TraceFinder software	Thermo Fisher Scientific	Version 4.1

RESOURCE AVAILABILITY

Lead contact

Further information and requests for resources and reagents should be directed to and will be fulfilled by the lead contact, Johannes Meiser (Johannes.meiser@LIH.LU).

Materials availability

No unique reagents were generated in this manuscript.

Data and code availability

- Data reported in this paper will be shared by the lead contact upon request.
- This paper does not report original code.
- Any additional information required to reanalyze the data reported in this work paper is available from the lead contact upon request.

EXPERIMENTAL MODEL AND STUDY PARTICIPANT DETAILS

Cell lines culture

MDA-MB468, 4T1, MDA-MB-231, HCT116, LN-229 and B16-F10 were cultured in DMEM (Thermo Fisher Scientific, A1443001) supplemented with 17.5 mM glucose, 2mM glutamine and 10% FBS. BT20 were cultured in advanced DMEM/F12 (Thermo Fisher Scientific, 12634010) supplemented with 2 mM glutamine and 10% FBS. A375 and SKMeL28 were cultured in RPMI 1640 (Thermo Fisher Scientific, 61870010) supplemented with 10% FBS. All cells were maintained at 37°C and 5% CO_2 and routinely tested for mycoplasma contamination. Serine/glycine starvation experiments were carried out using customised DMEM (Thermo Fisher Scientific, lot No. GME11933004) without phenol red, glucose, serine, glycine, tryptophan, pyruvate and glutamine with the missing ingredients added

according to the concentrations present in full DMEM and experimental setup. All experiments (except anchorage independent growth assays, see below) were seeded on D-1 and cells were allowed to adhere and attach overnight. Medium was aspirated and experimental medium plus treatment was added for the indicated time points in figures.

MDA-MB-468 WT and MTHFD1L-KO were received from Lewis Cantley lab, Weill Cornell Medical College, USA.[56] STR profiling in our lab in 2021 authenticated MDA-MB-468. LN-229 WT and AMPK-dKO cells were obtained from Michael Ronellenfitsch, Dr Senckenberg Institute of Neurooncology, University Hospital Frankfurt, Goethe University and have been previously described in,[48] B16-F10, A375 and SKMeL28 cells were received from Stephanie Kreis lab, University of Luxembourg, Luxembourg. 4T1 and BT20 were received from Clement Thomas lab, Luxembourg institute of Health, Luxembourg. MDA-MB-231 were obtained from Alexei Vasquez lab, Beatson Institute of Cancer Research, UK. All cell lines were originally purchased from ATCC.

Animal experiments

All experiments involving laboratory animals were conducted in a specific pathogen-free animal facility with the approval of the animal welfare structure of LIH and the Luxembourg Ministry for Agriculture, Viticulture and rural development under the references LUPA 2021/08 and LUPA 2021/22. Mice were treated in accordance with the European Directive 2010/63/EU. C57BL/6 mice were purchased from Janviers Labs (France).

TCL1-355 adoptive transfer

The TCL1-355 murine cell line was kindly provided by Dr Efremov.[51] A total of 2,000 TCL1-355 cells resuspended in DMEM without phenol red were injected intravenously (iv; 100 μL) in the tail vein of C57BL/6 mice. CLL progression was monitored by determining the percentage of $CD5^{+}CD19^{+}$ circulating CLL cells in the peripheral blood using flow cytometry. 14 days after iv injection, leukemic mice and age matched control mice were anesthetized with 2.0–2.5% of isoflurane and continuously infused with [U-^{13}C]glucose (50% solution in 0.9% NaCl) for 2h at a constant rate of 1.8 g/kg/h via the tail vein. At the end of the infusion, mice were euthanized via cervical dislocation and blood, organs and cells collection was rapidly performed.

Blood sampling was performed before and after infusion. Plasma was collected after two successive centrifugations at 1000 RCF for 10 min. B cells were isolated from the spleen. Briefly, suspension of splenocytes was prepared using gentleMACS Dissociator (Miltenyi). Then, B cells isolation (negative sorting) was performed using MojoSort Mouse Pan B Cell Isolation Kit II (Miltenyi), according to manufacturer's instructions. Cells were counted prior to pelleting and snap freezing. Pieces of spleen were also snap frozen in liquid nitrogen for metabolomics.

B16-F10 subcutaneous model

A total of 250,000 B16-F10 cells resuspended in PBS were injected subcutaneously (100 μL) into the flank of C57BL/6 mice and tumors were allowed to grow for 16 days for one group and 9 days for the second group. At endpoint, both groups were infused with [U-^{13}C]glucose as described above. After infusion, mice were euthanized with cervical dislocation and blood was collected into heparin tubes to separate plasma. Plasma and tumor tissue were snap frozen in liquid nitrogen.

METHOD DETAILS

Chemicals

Galactose, glucose, serine, glutamine and glycine were purchased from Sigma Aldrich and stock solutions were prepared in ^{MQ}water. BI-4916 and TEPP-46 were purchased from MedChemExpress and stocks were prepared in DMSO. BI-4916 was always used at a final concentration of 15μM while TEPP-46 was used at 100μM.

Lentiviral mediated knockdown of *PCK2*

The procedure followed was described in detail in.[26] For silencing *PCK2* gene in MDA-MB-468 cells, pGIPZ shPCK2-2: ATTATTGGACAGTCTTTGT (V3LHS_410309) vector plasmid purchased from Horizon Discovery was used.

CRISPR/Cas9 KO of *Pck2, MTHFD2, ALDH1L2*

MDA-MB-468 cells harboring deletion of MTHFD2 have been previously generated in.[26] To knockout *Pck2* in 4T1 and B16-F10, we used the same procedure described in[26]; two different gRNAs were used: 1. TATGCGTATTATGACCCGCC (Vector ID: VB211125-1122kdb, gRNA #654) to generate 4T1 clone A9 and B16-F10 clone A5. 2. GCGGGTCATAATACGCATAC (Vector ID: VB211125-1123gfv, gRNA #653) to generate 4T1 clone B7 and B16-F10 clone A9. For *ALDH1L2* deletion in MDA-MB-468 cells the same procedure in[26] was utilised with two different gRNAs: 1. GCAGAAGCCTACAGATCCGT (Vector ID: VB190719-1044jbf, gRNA #1529) to generate MDA-MB-468 clone F11. 2. GCGCTCCGGCGCTTCTCCAC (Vector ID: VB190719-1054khg, gRNA #1st Exon) to generate MDA-MB-468 clone D1.

Western blot

KOs and KDs cell pellets were directly obtained from cell culture by pelleting cells at 350 RCF for 5 min followed by a PBS wash and then freezing at −20°C awaiting cell lysis. Probing protein expression after treatments: cells were cultured at 150,000 cells/well density in a 6-well plate on D-1. At time point of extraction, the plate was placed on ice, medium was aspirated and cells were washed in

ice-cold PBS. Cell lysis buffer (150 mM NaCl, 1 mM EDTA, 50 mM Tris-HCl, 1% NP-40 with proteases and phosphatases inhibitors (Roche)) was added directly to the wells and cells were scraped and collected in pre-cooled Eppendorf tubes followed by sonification for 10 min. Lysates were spun at 16,000 RCF, 4°C for 10 min, the supernatant was collected in new tubes and the concentration of protein was determined with a Bradford assay. 20–40 μg of total protein was loaded into 15-well or 12-well RunBlue 4–12% Bis-Tris gels (GenScript) with the addition of 10mM DTT (Sigma Aldrich) and 4x NuPage LDS Sample buffer (Thermo Fisher Scientific) and gels were run for 90 min at 120V. Protein bands were blotted onto nitrocellulose membrane for 2h at 30 V. Membranes were blocked using 5% milk powder in TBS-0.1% Tween solution for 1h at RT. Membranes were incubated in the corresponding primary antibody overnight at 4°C and for 1h at RT in secondary antibodies. Detection of protein bands was done using Odyssey CLx Infrared Imaging system (LI-COR). Image StudioLite software Vers.5.2 (LI-COR) was used for quantifications and analysis. Primary and secondary antibodies used in this study are listed in the key resources table. All primary antibodies were used at 1:1000 dilution while secondary antibodies were used in a 1:10,000 dilution.

Flow cytometry analysis

Apoptosis

250,000 cells (MDA-MB-468, B16-F10 and A375) or 200,000 cells (4T1) were seeded in 6-well plate, allowed to attach overnight and treated as indicated for 48h. At endpoint, medium was collected, cells were washed with PBS and PBS was collected followed by cell trypsinisation. Cells were pelleted and washed with ice-cold PBS. Each sample was stained for 15 min on ice and in the dark with 50 μL AnnexinV staining solution (5% AnnexinV-FITC antibody in AnnexinV binding buffer (10 mM HEPES pH 7.4, 140 mM NaCl, 2.5 mM $CaCl_2$, 0.1% BSA in ^{MQ}water)). Directly prior to measurements, 450 μL of propidium iodide (PI) staining solution was added (11.1 μg/mL in AnnexinV binding buffer). Measurements were done using NovoCyte Quanteon flow cytometer (Agilent) and software NovoExpress (version 1.5.0). FlowJo version 10.6.2 was used for analysis.

ROS measurements

MDA-MB-468 cells were seeded at a density of 250,000 in a 6-well plate and left to attach overnight. After attachment, cells were treated as indicated with fresh DMEM containing either 17.5 mM glucose or 17.5 mM galactose alone or supplemented with 5mM N-acetylcysteine (NAC). A positive control well was treated with either glucose or galactose DMEM and 100 μM of H_2O_2 and cells were incubated for 24 h at 37°C and 5% CO2 in a humidified incubator. At endpoint, medium was aspirated, cells were washed followed by cell trypsinisation. Cells were pelleted and washed with PBS. The cell pellet was resuspended in 200 μL of H_2DCFDA at a final concentration of 10 μM in DMEM without FBS and subsequently incubated for 30 min at 37°C and 5% CO2 in a humidified incubator. After staining, cells cere pelleted, washed with ice-cold PBS and resuspended in 500 μL of FACS buffer (1x PBS, 10% FBS, 2 mM EDTA). Tubes were protected from light until immediately before measurement with the NovoCyte Quanteon flow cytometer (Agilent) and software NovoExpress (version 1.5.0). FlowJo version 10.6.2 was used for analysis.

Proliferation assays

Cells were seeded at a concentration of 25,000 cells/well in a 12-well plate or 12,500 cells/well in a 24-well plate in triplicates. Separate triplicate wells were counted when treatment was added to set 0h count for fold change calculations. Medium and treatment were replaced at 48h and 72h. At endpoint, cells were trypsinised and viable cell count was obtained using Countess automated counter (Thermo Fisher). Growth rate in Figure S6A was calculated using the equation: [*ln*(final cell count/initial cell count)]/duration.

Anchorage independent 3D growth assays

Cells were cultured in ultra-low attachment flask (Greiner) for a minimum of five days. Cells were collected and spun at 100 RCF for 5 min and afterward resuspended in Ca^{+2} and Mg^{+2} free PBS. 5,000 cells were seeded in 96-well ultra-low attachment plates (S-Bio or facellitate) already in the experimental medium and the plates were spun at 100 RCF for 10 min. 3D growth was determined using IncuCyte S3 Live-Cell Analysis system (Sartorius) over the indicated time periods.

RNA extraction, cDNA synthesis and RT-qPCR

300,000 cells were seeded in 6-well plate and treated for 24h as indicated in the figures. RNA was extracted directly from the plates using RNeasy Mini Kit (Qiagen, 74104). 2μg of RNA were used for cDNA synthesis using High Capacity cDNA Reverse Transcription Kit (Thermo Fischer Scientific, 4368814). For qPCR, we used Fast SYBR Green Master Mix (Thermo Fischer Scientific, 4368814) with 20 ng cDNA/sample in triplicates or duplicates and the reaction was conducted at 95°C for 20 s followed with 40 cycles of 95°C for 1 s and 60°C for 20 s. The QuantStudio 5 Real-Time PCR System was used (Applied Biosciences, ThermoFisher Scientific). CT values were determined by QuantStudio Design and Analysis v1.5.1 software (Applied Biosciences, ThermoFisher Scientific). Fold change of mRNA expression was determined using ddCt algorithm. Primers used in this study are listed in Key Resources Table.

Metabolomics

Stable isotope tracing and metabolite extraction

In vitro tracing and metabolite extraction. Stable isotope tracing experiments with [U-^{13}C]glucose, [U-^{13}C]galactose, [U-^{13}C]glutamine, [U-^{13}C]serine, [U-^{13}C]Palmitic acid, [^{15}N-amine]L-glutamine (Cambridge Isotope Laboratories, CLM-1396, CLM-1570, CLM-1822, CLM-1574, CLM-409 and NLM-1016 respectively) and [U-^{13}C]lactate (Sigma Aldrich, 485926) were performed in DMEM

(Thermo Fisher Scientific, 1443001), RPMI 1640 for SILAC (Thermo Fisher Scientific, 88365), Advanced DMEM/F12 for SILAC (Thermo Fisher Scientific, A2494301) or customised DMEM (Thermo Fisher Scientific, lot No. GME11933004) depending on the cell lines used. These tracer mediums were supplemented with the missing metabolites according to the experimental setup to mimic the original formula of DMEM, RPMI 1640 or advanced DMEM/F12. For sodium [U-^{13}C]lactate, 5 mM final concentration was used. For glucose and galactose tracing 10% FBS was used while for the rest we used 10% dialyzed FBS. 17.5 mM concentration of glucose and galactose tracer was used in their respective experiments. For [U-^{13}C]palmitate tracing was done as described in,[58] in brief tracer powder was dissolved in 100% ethanol at 60 °C at a concentration of 20 mM. Palmitic acid was added slowly to 10% BSA solution at 37°C while shaking on a thermomixer at a ratio of 1:3 BSA. Once the solution was cleared, it was added to the complete medium at a concentration of 200 μM while using 10% charcoal-stripped FBS. Experimental set-up and extraction of metabolites for GC-MS analysis was done as described in.[26] Metabolite extraction for LC-MS was done as described in.[24] Metabolite extraction for IC-MS was identical to LC-MS.

In vivo metabolite extraction. Metabolite extraction from tumors, spleen and plasma was performed as detailed in.[24] The absolute quantification of glucose in plasma and spleen was performed using standard addition method. In brief, known concentrations of glucose were added serially to metabolite extracts of each sample. After measurements, a calibration curve was used to determine the concentration of glucose in the original samples by determining the absolute value of the x axis intercept.

For B cells separated from the spleen, cells were washed with ice-cold PBS and subsequently 40 μL/one million cells extraction buffer [acetonitrile/$^{MQ}H_2O$/methanol (ratio, 3:2:5); liquid chromatography–MS (LC-MS) grade solvents] was added to each cell pellet. Cells were mixed for 10 min on a thermomixer at 4 °C at maximum speed, and then the tubes were centrifuged for 10 min at 16,100 RCF at 4°C. 50 μL of the supernatant was collected and transferred to an already-cooled LC-MS glass vial with inserts and stored at −80°C until measurement.

YSI measurements and medium exchange rates (Figure 2A; Figure S5A)

Medium samples were filtered (PVDF, 0.22 μm) prior measurement to remove particulates.

Absolute quantitative values for lactic acid and glutamine were acquired using a YSI 2950D Biochemistry Analyzer (Kreienbaum KWM). The instrument was calibrated and prepared according to the manufacturers' instruction. For a precise and reliable quantification, external concentration curves of each target compound were prepared and measured in triplicates. Absolute uptake and release rates were calculated as described in.[24]

GC-MS measurements

Formate measurements. Formate was derivatized to benzyl formate from the collected medium samples using the MCF protocol described in.[24] GC-MS analysis was performed using an Agilent 7890 A GC coupled to an Agilent 5975 C inert XL Mass Selective Detector (Agilent Technologies). A sample volume of 1 μL was injected into a Split/Splitless inlet, operating in split mode (20:1) at 280 °C. The gas chromatograph was equipped with a 30 m (I.D. 250 μm, film 0.25 μm) ZB-5MSplus capillary column (Phenomenex, 7HG-G030-11-GGA) plus 5 m GUARDIAN in front of the analytical column. Helium was used as carrier gas with a constant flow rate of 1.4 mL/min. GC oven temperature was held at 90 °C for 1 min and increased to 115 °C at 10 °C/min followed by 20 °C/min to 160 °C and a post run time of 4.25 min at 325 °C. Total run time was 10 min. Transfer line temperature was set to 280 °C. Mass selective detector (MSD) was operating under electron ionization at 70 eV. MS source was held at 230 °C and the quadrupole at 150 °C. For precise quantification, measurements were performed in selected ion monitoring mode. Target ions (m/z) and dwell times are listed below in Table S1. GC-MS chromatograms were processed using Agilent MassHunter Quantitative Analysis for GC-MS, Version B.08.00. Natural isotope correction and analysis of formate release rates was done as previously described in.[24]

Intracellular metabolites measurements (Figures S4A and S4C). First, dried polar extracts were derivatized for 90 min at 55 °C with 20 μL of methoxyamine (c = 20 mg/mL) in pyridine under continuous shaking and subsequently for 60 min at 55 °C with additional 20 μL of MTBSTFA w/1% TBDMCS. GC-MS analysis was performed using an Agilent 7890B GC coupled to an Agilent 5977 A Mass Selective Detector (Agilent Technologies). A sample volume of 1 μL was injected into a Split/Splitless inlet, operating in splitless mode at 270 °C. Gas chromatograph was equipped with a 30 m (I.D. 250 μm, film 0.25 μm) ZB-35MS capillary column with 5 m guard column (Phenomenex). Helium was used as carrier gas with a constant flow rate of 1.2 mL/min. GC oven temperature was held at 100°C for 2 min and increased to 300 °C at 10 °C/min and held for 4 min. Total run time was 26 min. Transfer line temperature was set to 280°C. Mass selective detector (MSD) was operating under electron ionization at 70 eV. MS source was held at 230°C and the quadrupole at 150 °C. For precise quantification of the MID, measurements were performed in selected ion monitoring mode. The derivative measured here was pyruvic acid 1MeOX 1TBDMS with target ions 174.0–180.1 [M-57 fragment] and dwell times of 15 ms. The MetaboliteDetector software package (Version 3.220180913) was used for mass spectrometric data post processing, quantification, MID calculations, correction of natural isotope abundance, and determinations of fractional carbon contributions.[57]

IC-MS measurements (Figures 1C–1I; S1A–S1E, S5F–S5G and S7K–S7M)

For the IC-MS measurements, polar extracts were analyzed as previously described[59] with the following adjustments. 50–75% of the total polar extract was dried overnight under vacuum. Dried polar metabolite pellets were reconstituted in 25 μL of water (Milli-Q Advantage A10) of which 20 μL was injected. For the ICMS system, we interfaced a Dionex ICS-6000+ ion chromatograph coupled with a QExactive high resolution mass spectrometer (Thermo Fisher Scientific). The guard, column, gradient settings, and suppressor type remained unchanged.[59] The electrospray ionization (ESI) was set as follows: spray voltage of 2.500 kV, auxiliary gas temperature

of 420°C, seep gas flow rate of 0, auxiliary gas flow rate of 15 units, and sheath gas flow rate of 50 units. The settings for acquisition of MS1 data were: m/z scan range of 80–750, resolution of 17500 at 200 m/z, automatic gain control (AGC) target of 1e6, and maximum injection time of 100 ms. Data were acquired using two micro-scans.

LC-MS measurements. Metabolite analyses were performed using a Vanquish Flex LC coupled to a Q Exactive HF mass spectrometer (Thermo Scientific). Chromatography was carried out with a SeQuant ZIC-pHILIC 5 μm particles column (150 × 2.1 mm) protected by SeQuant ZIC-pHILIC Guard (20 × 2.1 mm) pre-column. Column temperature was maintained at 45°C. The flow rate was set to 0.2 mL/min and the mobile phases consisted of 20 mmol/L ammonium carbonate in water, pH 9.2 (Eluent A) and Acetonitrile (Eluent B). The gradient was: 0 min, 80% B; 2 min, 80% B; 17 min, 20% B; 18 min 20% B; 19 min 80% B; 20 min 80% B (0.4mL/min); 24 min 80% B (0.4mL/min); 24.5 min 80% B. The injection volume was 5 μL. All MS experiments were performed using electrospray ionization with polarity switching enabled. The source parameters were applied as follows: sheath gas flow rate, 25; aux gas flow rate, 15; sweep gas flow rate, 0; spray voltage, 4.5 kV (+) / 3.5 kV (−); capillary temperature, 325°C; S-lense RF level, 50; aux gas heater temperature, 50°C. The Orbitrap mass analyzer was operated at a resolving power of 30,000 at 200 m/z in full-scan mode (scan range: *m/z* 75 … 1000; automatic gain control target: 1e6; maximum injection time: 250 ms).

Data from IC-MS and LC-MS measurements were acquired with Thermo Xcalibur software (Version 4.3.73.11) and analyzed with TraceFinder (Version 4.1). Natural isotope subtraction and subsequent analysis were performed as previously described using in-house scripts.[24]

Oxygen consumption rate measurements

10,000 cells (MDA-MB-468, 4T1 and MDA-MB-231) or 20,000 cells (HCT116) were seeded into 96-seahorse microplate (Agilent) on D-1. After attachment, glucose and galactose medium were added and cells were incubated for 24h. Basal OCR was measured using XF96 Extracellular Flux Analyzer (Seahorse bioscience, Agilent) following the manufacturer's protocol, Wave 2.6.0 software was used for analysis. OCR was normalised by the protein concentration of the corresponding wells following the protocol described in[60] and using a Bradford assay.

QUANTIFICATION AND STATISTICAL ANALYSIS

Unless stated otherwise, unpaired two-tailed student's t-test with Welch's correction was used throughout the presented study as statistical tests were always performed between two groups. GraphPad PRISM (9.5.0) was used to calculate the p value. In the present study, *in vitro n* is defined as one independent experiment with at least two replicate wells (except for protein lysates and RNA samples where single wells were used). For *in vivo* experiments, *n* is defined as a sample from one mouse. Further details on the data dispersion and presented error bars can be found in figure legends.